**MPHIL**

# Confined Photocatalysts in Mesoporous Silicas for Carbon dioxide photoreduction

Morteo Flores, Fabian

*Award date:*
2018

*Awarding institution:*
University of Bath

# Confined Photocatalysts in Mesoporous Silicas for Carbon dioxide photoreduction

*Fabian Morteo-Flores*

A thesis submitted for the degree of Master of Philosophy

University of Bath

Department of Chemical Engineering

June 2018



Supervisor Dr. Salvador Eslava

# ACKNOWLEDGEMENTS

I would like to thank my supervisor Dr. Salvador Eslava Fernandez for his support during my first year at the University of Bath.

I want to say thank you to all the people that helped me in the research and techniques that I used such as Dr. Remi Castaing, Mr. Fernando Acosta, Dr. Philip Fletcher, Dr. Gabrielle Kociok, Dr. Brigite Simoes Rodriguez, and Dr. Viorica Sebestyen.

This time in Bath was the most amazing of my life. I met a lot of wonderful people, including three magnificent persons Ida Amura, Miriam Regue, and Luz Medina thanks for all your help. And, to my incredible boyfriend Christian Kelsey. You were my support in this difficult time in Bath and you showed that the life is wonderful and very emotional. Thanks to you, I took my own decisions and I learned how to love someone.

Finally, I would like to thank the CONACYT scholarship Mexico. And to my parents for the support (financial and emotional) for this year in Bath. Thanks for everything.

## ABSTRACT

Photocatalytic reduction of $CO_2$ offers a solution to the depletion of fossil fuels and the high levels of atmospheric $CO_2$ exacerbating the global warming. It is, therefore, necessary to develop more efficient photocatalysts that utilize the solar energy and efficiently convert $CO_2$ to useful fuels. For this purpose, this MPhil focused on the development of perovskite catalysts supported on silica materials (SBA-15 and KIT-6) for the photoreduction of carbon dioxide ($CO_2$).

Silica supports SBA-15 and KIT-6 were synthesized by hydrothermal treatment and a subsequent calcination at 550 °C. After this, different semiconductors called perovskites (mixed oxides $MFeO_3$) were deposited on the support materials in varying amounts (5%, 10%, and 20%) to know the effect of the incorporation with the use of a sol-gel method. The perovskites selected were $LaFeO_3$, $BiFeO_3$, $AlFeO_3$, and $YFeO_3$ due to their suitable bandgap and promising photocatalytic response in the visible light. In addition, $TiO_2$ was also deposited to make a comparison about bandgap and future photocatalytic conversion.

Both SBA-15 and, KIT-6 were analyzed with $N_2$ adsorption-desorption and XRD showing cylindrical pores with a diameter of around 7 nm and high specific surface areas. These characteristics make the supports good candidates to be a host of metal oxides species, and their pore diameter is suitable to allow that the $CO_2$ molecules will be adsorbed without problems ($CO_2$ size=3.4 Å).

This work revealed that the incorporation of species into the silica support resulted in a high loss of specific surface area. The inclusion of $TiO_2$ into the support had a different effect in comparison with the perovskites due to the Ti species reacted with the particle surface of silica materials preventing the dispersion inside of the channels of the support. The perovskites, however, were well dispersed provoking changes in the internal support structure observed for example in the pore diameter sizes. XRD confirmed the formation of most perovskites and $TiO_2$, except $AlFeO_3$.

Bandgap calculation from UV-visible spectroscopy measurements suggested that the bandgap of the perovskites in the silica supports increased due to their nanoconfinement, while $TiO_2$

bandgap did not change much due to poor nanoconfinement. Calculations on conduction and valence bands revealed that best samples for $CO_2$ photocatalytic reduction were the $LaFeO_3$ (KIT-6, and SBA-15) at 5%, and $YFeO_3$ supported at 5% and 10% wt loading on SBA-15 since both resulting materials have bandgaps in the visible range and conduction and valence bands straddling the redox potentials for $CO_2$ photocatalytic reduction with water ($CO_2/CH_3OH$)

In conclusion, the synthesis of ferrite perovskites nanoconfined on mesoporous silicas SBA-15 and KIT-6 have been investigated following impregnation with a sol-gel process. The results indicate that $LaFeO_3$, $BiFeO_3$, and $YFeO_3$ ferrite perovskites can be incorporated in SBA-15 and KIT-6 mesoporous silicas. Properties such as specific surface area and UV-vis absorption strongly depend on the amount of perovskites used. The samples $LaFeO_3$ (KIT-6, and SBA-15) at 5% and $YFeO_3$/SBA-15 supported at 5% and 10% were identified as the best candidates of the investigated catalysts for $CO_2$ photocatalytic reduction.

**INDEX**

## TABLE INDEX



## FIGURE INDEX

# LIST OF ABBREVIATIONS

| | |
|---|---|
| CB | Conduction band |
| CO | Carbon monoxide |
| $CO_2$ | Carbon dioxide |
| $D_p$ | Pore diameter |
| e- | Electron |
| Eg | Energy bandgap |
| GC | Gas chromatography |
| $h^+$ | Holes |
| IUPAC | International Union of Pure and Applied Chemistry |
| $O_{br}$ | Bridging oxygen |
| P123 | Pluronic 123 |
| PEO | Poly (ethylene oxide) |
| PPO | Poly (propylene oxide) |
| PSD | Pore size distribution |
| $S_{BET}$ | Surface specific area |
| TCD | Thermal conductivy detector |
| TEOS | Tetraethyl orthosilicate |
| $TiO_2$ | Titanium dioxide |
| UV-vis | Ultraviolet visible |
| VB | Valence band |
| $V_o$ | Oxygen defeat surface |
| $V_P$ | Pore volume |
| XRD | X-ray diffraction |

# 1. INTRODUCTION

Energy is an indispensable factor for the people, but the most significant problem is that we are exploiting large amounts of it. Fossil fuels are an essential help for the production of some products such as steel, cement, etc., and nearly 80% of the energy supply of the world is based on these fuels.[1] The consumption of fossil energy produces a global problem, and it is expected to face a severe crisis because of large volumes of production of carbon dioxide ($CO_2$).[2]

The supply of secure, clean and sustainable energy is the most significant challenge that the people face in the 21st century. However, unlike the power generation, it is not possible to substitute renewable energy sources for fossil fuels to reduce emissions such as $CO_2$. These emissions are mostly accumulating in the atmosphere, although the future effects of these emissions are still uncertain. Among renewable energy resources, solar energy is by far the most significant exploitable resource. It constitutes the primary power source on earth providing more energy in one hour than all the renewable energy produced in one year.

Solar fuels are compounds that have captured and stored solar energy in chemical energy. One example of this is the natural photosynthesis, where the sun is used as energy to carry out some useful reactions.[3] The process of natural photosynthesis is a combination of water oxidation and carbon dioxide reduction (or $CO_2$ fixation) reactions under bright and diffuse light conditions by which plants convert $CO_2$ of the atmosphere and water accompanied with oxygen ($O_2$) and other carbon products.[4]

Artificial photosynthesis only mimics the activity and the use of $CO_2$ with the use of semiconductors, and water to produce fuels such as hydrogen. Research into artificial photosynthesis processes have increased in recent years due to the problems of global warming and decreasing of fossil fuels reserves.[5] The challenge to reduce costs compared with fossil energy as the materials need to be very inexpensive to make a solar based process economical.

This Mphil focusses on the preparation of new materials which can be employed in photoreduction to convert $CO_2$ into solar fuels. Two mesoporous silica supports were selected due to their inert and mechanically high stability as well as high in the surface area and large

pore size. The selection of different semiconductors (called perovskites) was studied to incorporate into the matrix of the silica support at different amounts.

Techniques such as $N_2$ physisorption and X-Ray diffraction were realized to determine the physical and textural properties of these materials. UV-visible spectroscopy was performed as well to learn the bandgap of the samples and to obtain an idea about the probable products to achieve considering the redox potentials of $CO_2$ and the band edges.

The specific aims of this MPhil are:

- Develop new materials along the use of two mesoporous silica supports (SBA-15 and KIT-6) for using in the photoreduction of $CO_2$ into solar fuels ($CH_3OH$).
- Study of different perovskites ($LaFeO_3$, $BiFeO_3$, $YFeO_3$, and $AlFeO_3$) at various amounts (5%, 10%, and 20%) inside the silica support. This will help to determine the final product and to obtain a better catalytic performance.
- Perform characterization to study the physical and textural properties of the materials such as $N_2$ adsorption-desorption, X-Ray diffraction (XRD), and UV-visible.
- Analyze and compare the results with the properties of $TiO_2$ catalyst.

# 2. BACKGROUND

## 2.1. Carbon dioxide ($CO_2$)

Carbon dioxide ($CO_2$) is a gas formed by a central carbon and two atoms of oxygen, (figure 1) where the molecules are covalently bonded (O=C=O). Among its physical properties include non-flammable, colorless, odorless gas, acidic odor, density around 1.98 kg/m$^3$, and its molecular weight is 44.01 g/mol.[6]

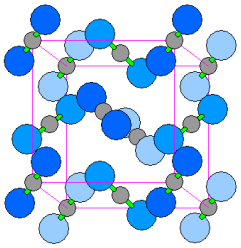

**Figure 1.** $CO_2$ (Carbon dioxide) structure, oxygen atoms are in blue bond to the grey circle (carbon)

The amount of $CO_2$ has been increasing in recent years due to the growing emissions from fossil fuel combustion. Emissions of this gas have accelerated activities to convert it as a carbon source for the production of fuels and chemicals.[7] There are three approaches to reduce $CO_2$ emissions. 1) efficient use of carbon-based power sources, 2) use of alternative carbon-free energy source and 3) use of a post-treatment carbon-capture technology.[8] However, the main problem is that $CO_2$ is a very stable molecule due to its thermodynamic stability and kinetic inertness. The transformation of $CO_2$ can be achieved via in two routes:

1) The feeding of a high-energy reactant (e.g., $H_2$), unsaturated compounds and organometallic compounds.
2) The supply of external energy such as solar or electrical energy.

In brief, the photocatalysis (PC) and photoelectrocatalysis (PEC) are two highly attractive routes for the reduction of $CO_2$.

### 2.2. Carbon capture and storage (CCS)

One step toward reducing $CO_2$ emissions is to capture the carbon dioxide emissions generated during combustion and store them in an adequate place. This process of carbon capture and storage, sometimes called CCS, has the potential to reduce future world emissions from energy by 20%.[9] In CCS, $CO_2$ is captured from power plants and then injected underground into reservoirs. While it may be critical for the continued use of fossil fuels in a carbon-constrained world, there is a broad political consensus that the global temperature rise should be limited to 2°C.

The scientific analysis defines that $CO_2$ must start to fall from 2020 onward. However, CCS is inevitable if the fossil fuels continued to be burned at more than 10% of all the present rate. The combustion of fossil fuels supplies more than 85% of energy for industrial activities and is the main greenhouse gas contributor. Coal will provide 28% of the global power by 2030, as part of a 57% increase in $CO_2$ emissions.

Although current CCS technology is only in the initial phase, the scale of the ambition to reduce $CO_2$ emissions by 20% is massive. Capture technologies allow the separation of carbon dioxide from gases produced in electricity generation. This technique can be achieved by one of three methods pre-combustion capture, post-combustion capture, and oxyfuel combustion. $CO_2$ is then transported by pipeline for storage where millions of tonnes of carbon dioxide are already carried annually for commercial purposes.[10] This scheme is illustrated in Figure 2.

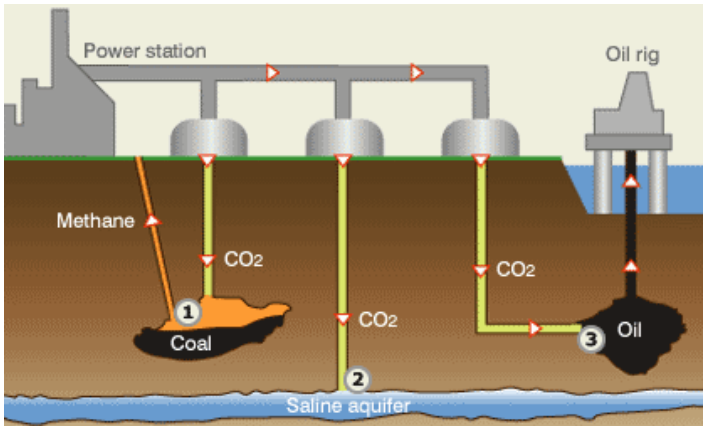


**Figure 2.** Carbon capture and storage (CCS) process.[11]

## 2.3. Photocatalytic $CO_2$

Photocatalytic $CO_2$ is known as one of the most favorable renewable energy technologies because of the ability to convert carbon dioxide with water into different solar fuels such as $CH_4$, $HCO_2H$, and $CH_3OH$. The process consists of the addition of one or more electrons to a photoexcited species. However, this technology is still limited by its small solar conversion efficiency due to the fast recombination of electrons ($e^-$) and holes ($h^+$), moderate charge consumption and the low adsorption of the $CO_2$ at the catalytic site.[12] The catalysts such as semiconductors improving the photocatalytic reduction of $CO_2$ with water. These semiconductors involve several main steps in the $CO_2$ photoreduction with $H_2O$ (Figure 3).[13,14]

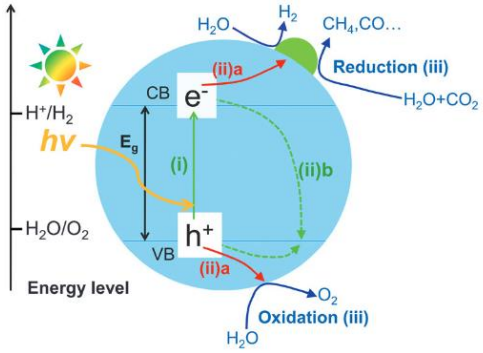


**Figure 3.** Schematic illustration of the mechanism of reduction of $CO_2$ with $H_2O$ on a semiconductor.[15]

1) Electrons (e-) and holes (h+) pairs are generated when the semiconductor photocatalyst is irradiated by the energy of a light source that it is equal or greater than the band-gap energy ($E_g$) of the utilized material.
2) The band-gap excitation (photoexcitation) leads to the formation of $e^-$ in the conduction band (CB) and $h^+$ in the valence band (VB).
3) After photoexcitation, the electron-hole pairs should be separated partially, and be transferred to redox active species across the interface and minimize electron-hole recombination. A significant fraction of $e^-$ and $h^+$ pairs recombine together with the energy being released in the form of heat or photons.
4) Once $e^-$ and $h^+$ are created, they can migrate to the surface and be trapped at the trap sites or recombine at the surface of the semiconductor.

5) Simultaneously, $H_2O$ is oxidized by the $h^+$ to produce $O_2$ and e- could migrate to the surface and reduce $CO_2$ to solar fuels if surface adsorbates possess a redox potential appropriate for a thermodynamically allowed reaction.

Reduction of $CO_2$ is an ascending reaction where CB and VB of the photocatalyst should straddle the reduction potential of $CO_2$ and the oxidation potential of water respectively. A higher CB edge relative to the reduction potential of $CO_2$ facilitates the transfer of electrons from CB to $CO_2$ (vacuum level). A lower VB edge relative to the oxidation potential of water helps the transfer of holes from VB to water.

If a $CO_2$ photocatalyst CB and VB straddles the redox potentials of $CO_2$ and water, under the irradiation of light, the removal of electrons from VB to $CO_2$, as well from the water to VB are thermodynamically favorable. Electrons in CB reduce $CO_2$, whereas holes in VB oxidize water to oxygen. The formal reduction potentials of the reactions regarding thermodynamics with the photoreduction of $CO_2$ and $H_2O$ versus normal hydrogen electrode (NHE) are given in Table 1.

**Table 1.** $CO_2$ Reduction potentials

| ***Reaction*** | $\boldsymbol{E^o\ (V)\ vs\ NHE\ (pH = 7)}$ |
|---|---|
| $\boldsymbol{CO_2 + 2H^+ + 2e^- \rightarrow HCOOH}$ | -0.58 |
| $\boldsymbol{CO_2 + 2H^+ + 2e^- \rightarrow CO + H_2O}$ | -0.53 |
| $\boldsymbol{CO_2 + 4H^+ + 4e^- \rightarrow HCHO + H_2O}$ | -0.48 |
| $\boldsymbol{CO_2 + 6H^+ + 6e^- \rightarrow CH_3OH + H_2O}$ | -0.38 |
| $\boldsymbol{CO_2 + 8H^+ + 8e^- \rightarrow CH_4 + 2H_2O}$ | -0.24 |

From a thermodynamic view, the creation of methane and methanol are more favorable in $CO_2$ reduction due to these reactions take place at lower potentials. However, the kinetic makes methane and methanol formation harder than carbon monoxide. Moreover, the 2-8 electrons and protons reactions to obtain the desired products are difficult.

UV radiation commits less than 4% while visible light accounts for more than 40% of sunlight, from 400 nm to 800 nm (3.12 – 1.56 eV).[16] A semiconductor should have a sufficient bandgap to fit the spectral absorption of visible light. As well, it needs to have its conduction band above the reduction potential of $CO_2$ facilitate the electron transfer. The measurement of the bandgap

of materials is essential in the semiconductor. Bandgap energy is significant in insulators (> 4 eV) but lower for semiconductors (< 4 eV).

The photocatalysts involve photoreactions which occur at the surface of a catalyst. These reactions can be carried out in two ways:

1. When the initial photo-excitation takes place in an adsorbate molecule, which then interacts with the ground state of the catalyst substrate, the process is referred to a catalyzed photoreaction.
2. When the initial photoexcitation takes place in the catalyst substrate, and the photoexcited catalyst then interacts with the ground state adsorbate molecule, the process is a sensitized photoreaction.[17]

Annual anthropogenic $CO_2$ emissions from fossil fuel combustion have a current level of $CO_2$ in the atmosphere about 400 ppm, approximately 43% higher than the level recorded in pre-industrial times. $CO_2$ reduction efficiency is generally low, many of the carbon products detected may not have originated from photoreduction. Although its low efficiency, artificial photosynthesis of $CO_2$ to fuel has become an attractive route due to its economically and environmentally friendly behavior. From an economic and environmental point of view, recycling of $CO_2$ to fuels such methane under solar irradiation mimics natural photosynthesis without using extra energy and there is no destructive effect on the environment.

This technology has some difficulties and barriers due to the non-effective catalysts, low yield, and selectivity. But, the approach of the semiconductor photocatalysts offers great potential for transforming earth-abundant materials into high energy density chemical via complex photoreactions that harness solar photons represents an exciting opportunity. This is, therefore, a far more attractive approach from a sustainability perspective.[18,19]

### 2.4. Band theory

The description of the states of electrons in an atom is according to their four quantum numbers. When an atom is combined to form substances, the orbitals merge providing a high number of energy levels for electrons. When large numbers of particles are close to each other, the

available energy levels form a nearly continuous band where the electrons may move (see Figure 4)

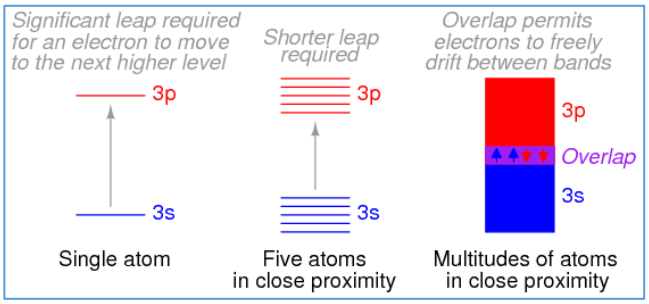


**Figure 4.** Description of bandgap

In some substances, a considerable gap remains between the highest band containing electrons (called valence band) and the band with no electrons (called conduction band). These materials that fall within the category of semiconductors have a narrow gap between the valence and conduction bands, where an amount of energy is needed to remove an electron from the valence band to a higher unoccupied band. So the electronic band structure of solids can explain the distinction between metals, insulators, and semiconductors.[20] The difference of electronic band structures of the three solids is shown in Figure 5.

- **Metals:** They are excellent conductors since the valence and conduction bands overlap in metals, little energy removes an electron.
- **Insulators:** The large gap between the valence and conduction bands of an insulator requires high energy to remove an electron. Thus, insulators do not conduct.
- **Semiconductors:** They have a small non-overlapping gap between the valence and conduction bands. Pure semiconductors are neither excellent insulators nor conductors. Semiconductors are semi-conductive.

An important parameter in the band theory is the Fermi level, the top of the available electron energy levels at low temperatures. The position of the Fermi level with the relation to the conduction band is a crucial factor in determining electrical properties.

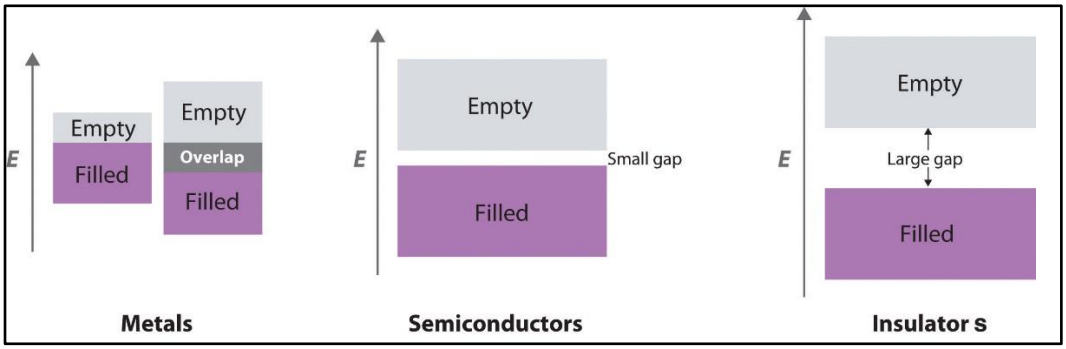


**Figure 5.** The difference of electronic band structure of solids.[20]

## 2.5. Semiconductor

A semiconductor has a favorable combination of electronic structures, light absorption, and charge transport because its energy gap (bandgap) exists between the top of the filled (valence band) and the bottom of the vacant (conduction band). The semiconductor can form photoinduced electrons and holes upon irradiation, a phenomenon governed by the band energy position.[21]

There are two types of semiconductors: p-type and n-type.[22]

- The p-type semiconductors have a significant hole concentration higher than electrons. The term p-type refers to the positive charge of the hole where the holes are majority carriers. In these, the impurity of some trivalent element (such as boron, aluminum, Indium, Galium, etc.) can accept one electron (acceptor semiconductor). For these semiconductors, the Fermi level lies closer to the VB than the CB.

- The n-type semiconductors have a larger electron concentration compared to that of holes. The term n-type comes from the negative charge of the electron. In these semiconductors, the impurity of some pentavalent element such as Phosphorus, Bismuth, etc., in this case, the impurity atom donates one electron, (donor semiconductor). In this case, the Fermi level is higher and lies closer to the CB than the VB.

## 2.6. Photocatalytic supports

In addition to semiconductor catalysts, some porous materials such as zeolites, silica mesoporous can also be utilized in photocatalytic reactions. Such porous materials with a high surface area, tunable porosity, and dimensionalities are suitable for capturing small $CO_2$ or $H_2O$ molecules in their cavities.[23,24] The incorporation of $CO_2$ reduction sites into these porous materials is a promising strategy to provide a suitable catalyst structure, in which $CO_2$ can be efficiently adsorbed, activated and reduced by photogenerated electrons.

Ikeue et al.[25] studied a series of $CO_2$ photoreduction reactions over 3D dimensional support containing highly dispersed $TiO_2$. They incorporated $TiO_2$ species into the framework of the support by hydrothermal synthesis and performed $CO_2$ photoreduction with $H_2O$ to produce $CH_3OH$ in the gas phase over the obtained catalysts. The previous results are because of the formation of charge transfer excited complexes of $Ti^{3+}$ -$O^-$ under the UV irradiation on the isolated $TiO_2$ species in the framework.

These results indicated that the structure with large pore sizes having a three-dimensional channel structure was suitable not only for achieving high dispersion state of the $TiO_2$ species. But also, for achieving a large amount of adsorbed $CO_2$ and a high efficiency to generate $CH_3OH$. The increase of $CO_2$ photoreduction activity was ascribed to the larger pore size and the resulting higher dispersion of $TiO_2$ species in Ti-SBA-15. The utilization of mesoporous materials (MCM-41, SBA-15, KIT-6, etc) for highly dispersed $TiO_2$ species leads to relatively high efficiency for $CO_2$ photoreduction into $CH_3OH$, which makes them promising candidates for $CO_2$ photoreduction.[26]

It is known that light harvesting process is strongly dependent on the surface of the photocatalyst. It usually improves through the incorporation of macroporous or mesoporous architectures for the utilization of light. The surface area of a photocatalyst can be enhanced by dispersing in a porous support. The support moreover can define the potential, chemistry of immobilization strategies and the control of the surface reactivity.

Mesoporous materials are one of the types of porous materials according to IUPAC with a pore diameter in the range of 2-50 nm. These mesoporous supports are made up of pore walls, which

have ordered arrays of uniform nanochannels and high surface area (600-1300 $m^2/g$).[27] A transparent porous silica material is an extraordinary support for $TiO_2$ photocatalysts, due to its low cost, availability, mechanical robustness and the high surface area. It can improve photocatalyst dispersion and increase adsorption of $CO_2$ and $H_2O$ on the catalyst.[28] Silica consists of entirely condensed silanoxy bridges (=Si-O-Si=) in the framework and silanol functional groups on the surface.[29] Pure mesoporous silica can be found in three structure types:

- Hexagonal (1D regular hexagonal of mesopores channels)
- Lamellar (2D system of silica sheets interleaved)
- Cubic (3D bicontinuous network of pores)

The mesoporous materials are based on the arrangement of pores, ordered or disordered, in an amorphous framework. This arrangement varies from 1D pores to 3D interconnected pores. Ordered mesostructures can be defined by space group symmetry, whereas disordered mesostructured have no such notation. The characteristic properties such as porosity and stability of disordered materials are comparable to those of ordered structures.

One question to resolve is what mesostructured material is superior 2D or 3D? This is difficult to answer due to the priority selection with respect to the characteristic of the pore. Among the most used and studied mesoporous supports made up of silica are SBA-15 and KIT-6, these supports are described below.[30–32]

### 2.6.1. SBA-15

SBA-15 (Santa Barbara amorphous) is a mesoporous silica material that has cylindrical pores ordered in a hexagonal structure where nanorods are interconnected by the network.[33] The pores are responsible for the high surface area that facilitates the diffusion of the reactants through the structure.[34] See Figure 6.

**Figure 6.** Structure of SBA-15

The silica structure is not a functional catalyst. It is a host or template for catalysts with nanoparticles or for adding functional groups to the silica structure. Its key features are:

- It can reach pore sizes of 30 nm in two dimensions
- It exhibits a wall thickness of 3 to 7 nm
- The length of the pores varies from 200 nm.
- Its wall thickness improves the thermal and hydrothermal stability in comparison with MCM-41 and related materials.
- Its surface area is around 800-1500 $m^2/g$ more than the conventional $TiO_2$.

Yang et al.[35] studied the semiconductor $TiO_2$ embedded in the mesoporous SBA-15 for photocatalytic activity. Their studies showed much higher photodegradation ability than pure commercial $TiO_2$ (P-25). Experimental results indicated that the photocatalytic activity of titania/silica mixed materials depends on the adsorption ability of the composite and the photocatalytic activity of titania.

### 2.6.2. KIT-6

KIT-6 has a three-dimensional cubic la*3*d symmetry with a complex pore geometry and two sets of independent channels which are separated by an amorphous silica wall as illustrated in Figure 7.[36,37] Due to its unique properties related to a 3D channel network, it provides highly opened spaces for direct access to guest species without pore blockage and immobilization of large molecules.[38] Its main features are:

- It consists of ellipsoidal cages that are 3D connected by smaller cage connecting pores.

- It possesses large readily tunable pores with thick pore walls.
- High hydrothermal stability.
- High surface area (between 600 to 800 $m^2/g$) and a large pore volume.

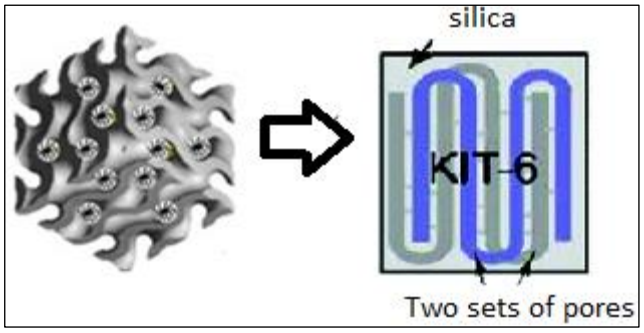


**Figure 7.** Structure of KIT-6.[36]

2D ordered porous materials possess narrow pore size distribution, tunable porosity, high surface area, and a broad range of molecular size for adsorption and for active compound release properties. Meanwhile, 3D disordered porous materials are ruled by the randomness, connectivity, and tortuosity of the pore space. Both materials use cost-effective silica source that would be the best choice in the synthesis of large pore mesoporous silicas for industrial application.[39]

### 2.6.3. Synthesis of mesoporous silica support

Mesoporous silica is obtained by the addition of an organic template surfactant to the synthesis of $SiO_2$. The synthesis of the mesoporous silica is called sol-gel method because the solution (sol) is a colloidal system where micelles are formed by surfactants dispersed in an aqueous solution. A surfactant is an amphiphilic molecule that is composed of hydrophilic and hydrophobic parts. The hydrophilic component (lipid soluble in water) is sometimes a hydrocarbon chain that helps to form micelles.

Several surfactants can be used in the mesoporous silica synthesis as cetyltrimethylammonium bromide (CTAB) and Pluronic 123 (commonly named P123). The use of block copolymers is one of the most promising routes regarding high degree of ordering and resulting in a material with excellent hydrothermal stability. Because of their rich phase behavior, low cost and non-toxic degradation.[40] Pluronic polymers (P123) consist of a hydrophobic polypropylene oxide

block (PPO) surrounded by two hydrophilic polyethylene oxide blocks (PEO) and can be written as $(PEO)_X$-$(PPO)_Y$-$(PEO)_X$. The hydrophilic polymers favor the hexagonal phases or even cubic of the most hydrophilic polymers with long PEO chains.[41] The formation of SBA-15 is proposed in three stages, the micellar formation, hydrothermal process, and calcination.[42]

- **Micellar formation**

In the initial stage of the synthesis, the direct structure agent (P123) is dissolved in aqueous media to give a micellar solution. The micelles are spherical with a core with PPO chains and a corona consisting of PEO groups (as shown in Figure 8). All this is described as the core-corona spherical model.

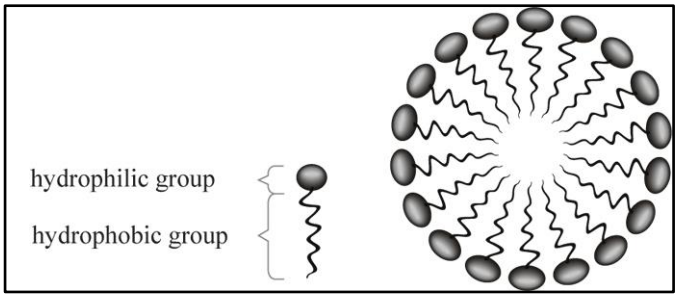


**Figure 8.** Micellar formation.[43]

Although the PEO chains are hydrophilic to ensure an amphiphilic character, the PEO corona is less polar; this results in a weak interaction between the O-Si-O groups and the PEO groups of the micellar corona.[44]

Organosilicates such as tetraethyl orthosilicate (TEOS) are used as the source of silica. When it interacts with the water media, it hydrolyzes into silica acid and starts to condense and polymerize at 35 °C forming a silica network. The reason of this is the attraction between the silica and PEO. When the silica oligomer has grown, they have little contact with the micellar corona to cause the adsorption of it. TEOS is better to put before the emulsion to avoid the formation of free silica spheres.

- **Hydrothermal treatment**

The aim of the hydrothermal treatment is the formation of the hexagonal structure which begins when a white precipitate is created. This effect is due to the consolidation of the silica network by incubation of particles at a higher temperature (around 80 °C).

After the addition of silica, the micelles core-corona increases in electron density and the arrangement of the surfactants micelles create a mesosphere whose structure is determined by weak forces. The pluronic micelles join the adsorbed silica into flocs of micelles.[45] Next, the silica polymer disperses to destabilize the flocs, and they are associated with solid particles. Finally, there is a transition from Pluronic micelles into a cylindrical shape (rods) that rearrange into a hexagonal phase due to the attraction between silica and PEO that originates from silica polymerization.[46]

As time progress, the core-corona interface is reduced and increase silica polymerization in this region. The polymerization continues in the corona region where the polymerization starts and close to the core and then propagates out of the zone. When the temperature increases, the mesopores size, and the surface area increase in size and the microporosity decrease. After the surfactants are eliminated, an amorphous silica structure is obtained, and the intrawall porosity grows in size as result of PEO from silica.

- **Calcination**

The calcination of the particles around 500°C for 6 hours removes the organic polymer components (surfactants), and the silica network is enhanced. At this stage, the hexagonal structural retains its size. Above 300 °C, the water from the structure is released, the rest of the organic polymers are burned out, and the hexagonal framework decreased as we can see in Figure 9. Finally, the mesopore volume decreases indicating the micropores are emptied from surfactants.[47] Upon the removal of the polymer, smaller pores (<2 nm) inside the silica wall are created as a cast of the PEO part. These small pores are called intrawall pores, and they connect to the primary mesopores, that is the reason that SBA-15 is a bicontinuous material.[48]

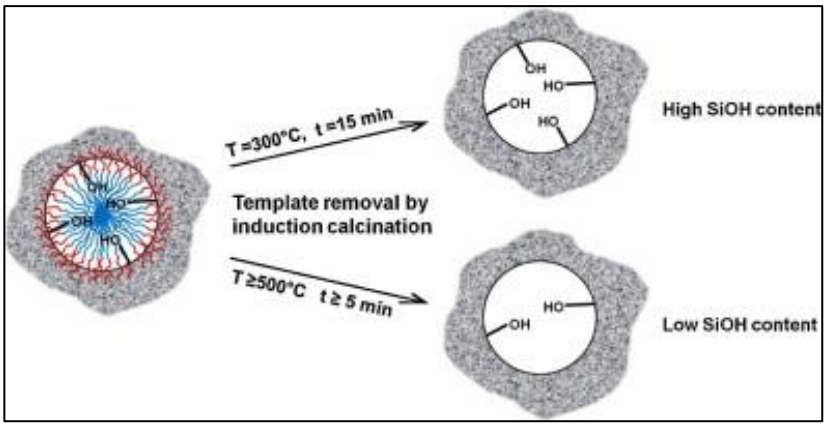


**Figure 9.** Surfactant removal from ordered mesoporous silica materials by calcination.

## 2.7. Titanium dioxide ($TiO_2$)

Titanium dioxide ($TiO_2$) is the most promising material for photocatalytic activities due to its chemical stability, low-cost and no risks to the environment.[49] $TiO_2$ is an n-type semiconductor existing in four polymorphs forms: anatase (tetragonal), brookite (orthorhombic), rutile (tetragonal) and $TiO_2$ (monoclinic) as illustrated in Figure 10. Thermodynamic calculations predict that rutile is the stablest phase at all temperatures.[50]

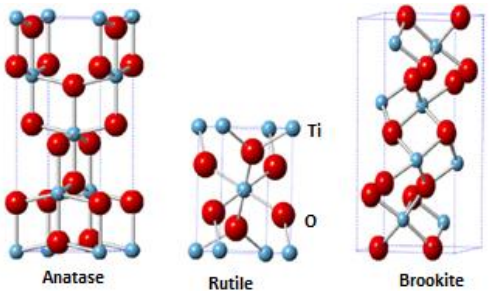


**Figure 10**. Crystal structure of anatase, rutile, and brookite.[51]

Several strategies have been used to improve the absorption ability of an inorganic photocatalyst, especially on $TiO_2$ since it is the most widely studied photocatalyst. They are described in the following paragraphs.

### 2.7.1. Metal deposition

The most employed modification method is to load nano-sized metals at $TiO_2$ surface by photodeposition impregnation. The surface metal nanoparticles significantly affect the

photochemical properties of $TiO_2$ support. Various metal nanoparticles such as Pt, Au, and Ag have been used in $TiO_2$ photocatalyst where Au and Ag have often been coupled to $TiO_2$ to utilize the property of localized surface plasmonic resonance (LSPR). This LSPR is the collective free electron charge oscillation in the metallic nanoparticles that are excited by light; this phenomenon strongly depends on particle size, shape, and local dielectric environment. See Figure 11.

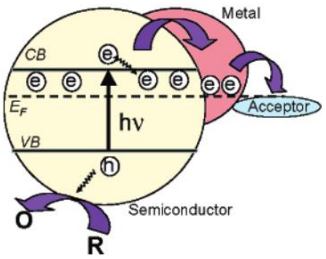


**Figure 11.** Semiconductor-metal nanocomposite system.[52]

Ku, Y et al., studied metallic platinum on $TiO_2$ particles. The dispersion of the metallic platinum was uniform, and it did not alter the morphology of the $TiO_2$ particles. However, the absorbance of the Pt/$TiO_2$ catalyst for light with wavelength more than 400 nm was much improved by the addition of metallic platinum. The decomposition and mineralization of acetone increased with the UV light intensity for experiments conducted in the photoreactor coated with Pt/$TiO_2$. The conclusion in this study revealed that the activity of $TiO_2$ by the deposition of a metal (Pt) increased due to the increase of electron transfer rate to the oxidant allowing visible light absorption and providing defect states in the bandgap.[53]

### 2.7.2. Doping

Doping with elements has been pursued to sensitize photocatalysts with a full bandgap toward visible light absorption. Doping with metal ions ($Fe^{3+}$, $Zn^{2+}$, etc.) and non-metal ions (C, N, S, B, etc.) have already been widely studied. This method does not only retard the fast charge recombination but also enable visible light absorption by creating defect states in the bandgap. CB electrons or VB holes are trapped in the defect sites inhibiting the recombination and increasing the charge transfer.[54] The mechanism of $TiO_2$ doped is illustrated in Figure 12.

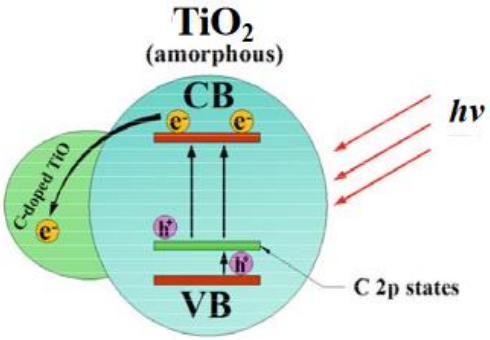


**Figure 12.** Photocatalyst mechanism of $TiO_2$ doped under visible light irradiation.[55]

### 2.7.3. Surface charge modification

The surface interaction with oxide semiconductors can influence the photocatalytic reaction rate and mechanism. Metal oxides such as silica, alumina, and zirconia are the standard inorganic surface charge modifiers.

Shariq et al. examined the effect of the photocatalytic degradation of aqueous pollutants using $SiO_2$-$TiO_2$ photocatalyst.[56] The results indicated that the surface properties of $TiO_2$ modified with silica-enhanced the degradation of cationic contaminants such as amines. These results were possible due to the increase of surface area and the introduction of Si-O groups which increased the adsorption on $TiO_2$. It only worked with cationic pollutants, not with anionic. These results also showed that a lower pH value (pH=6→3) affects the mobility of suspended $TiO_2$ particles.

### 2.7.4. Dye-sensitization of $TiO_2$

Coupling of organic dyes to the surface of $TiO_2$ has attracted much attention as a sensitization method for visible light utilization. During visible light irradiation, excited electrons are transferred from the dyes to the semiconductors. Advantages of the dye-sensitized photocatalytic reactions are the fast injection of electrons to the semiconductor and slow backward reaction. This response occurs only from the dye molecules adsorbed on the surface of the photocatalyst.[57] See Figure 13.

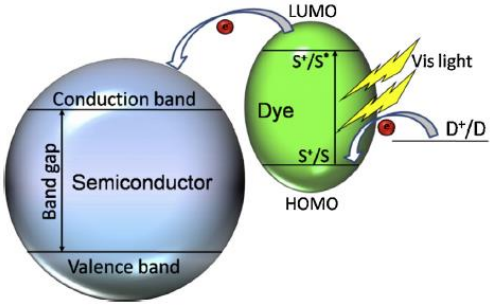


**Figure 13.** Mechanism of dye-sensitized semiconductor Photocatalysis.

Trenczek-Zajac et al. investigated a coupled system by mixing $TiO_2$ with CdS and its photocatalytic activity in UV-vis using methyl orange (MO).[58] It was demonstrated that small amount of CdS (5 mol%) or $TiO_2$ (5 mol%) in the nanocomposite improves the photocatalytic properties. The sensitization can be explained by the electron transfer from CdS grains to $TiO_2$ and the extended absorption of visible light. The highest photocatalytic activity under exposure to UV-vis light was obtained for the composition of 5 mol% $TiO_2$ and 95 mol% CdS.

$TiO_2$/Cds samples exhibited more desirable photocatalytic activity in visible light when compared to pure $TiO_2$ and CdS. These improved photocatalytic properties of the couple semiconductors are related to efficient charge transport between $TiO_2$ and CdS. The results reported the photodegradation of methyl orange in the presence of various $TiO_2$/CdS nanocomposites.

### 2.8. Perovskites

A perovskite is a type of mineral composed of calcium, titanium, and oxygen in the form of $CaTiO_3$. All materials with the same crystal structure are named perovskites ($ABX_3$). In this structure, A are positive ions at the corners of the unit, B are negative ions occupying the face position and X are oxygen.[59] Oxide perovskites form large families among the structures of oxide compounds. Their essential features are exceptional thermal stability, electronic structure, ionic conductivity, electron mobility, redox behavior and a wide range of Ferro, piezo and electrical properties.[60,61] The perovskite structure is illustrated in Figure 14.

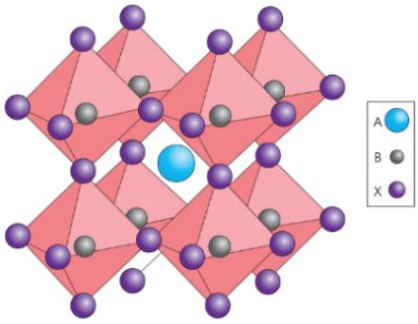


**Figure 14.** Schematic drawing of the crystal structure of perovskite.[62]

Several oxide perovskites have been developed with visible light activity. Various strategies have been employed for enhancing the photocatalytic performance emphasizing the advantages and challenges offered by these materials.[63] In the multiferroic materials, the electric and magnetic properties are mutually controlled, which enables their use in potential devices such as sensors and data storage.[64]

### 2.8.1 Ferrite Perovskites

Efficient energy conversion and storage often requires perovskites with a set of specific properties concerning their electronic, physical, and chemical natures. These requirements are so complex that more often than not we fail to find a candidate that can satisfy all the needs simultaneously for the $CO_2$ photoreduction. As a result, the lack of suitable materials has indeed become an important challenge in energy research.

The most commonly encountered form of iron oxide in nature, hematite is a semiconductor with and an almost ideal bandgap for $CO_2$ photoreduction. Hematite ($Fe_2O_3$) stands out as a suitable candidate due to due to its reported bandgap of 2.0-2.2 eV.[65,66] Moreover, hematite and other iron oxide compounds have known shortcomings such as short exciton diffusion length, low electron conductivity, and lower conduction band edge potential.[67] However certain ferrite-based perovskites have shown good photocatalytic activities, circumventing the shortcomings seen in binary iron oxides.[68]

This class of binary iron oxides compounds involves $MFeO_3$ perovskite-ionic ferrites which have a mixed electronic-ionic conductivity.[69] Some of the most important are: $LaFeO_3$, $BiFeO_3$, $YFeO_3$, and $AlFeO_3$, which are described in the following sections.

### 2.8.1. Lanthanum Ferrite ($LaFeO_3$)

$LaFeO_3$ is an essential p-type semiconductor with a narrow bandgap of 2.65 eV.[70] It has demonstrated excellent photocatalytic activity under visible light irradiation (Figure 15). Its crystal structure is orthorhombic, and its lattice parameters are a=5.556 Å, b= 5.565 Å, and c= 7.862 Å.[71] $LaFeO_3$ is well-known as a visible light photocatalytic active due to its unique optoelectronic property.[72]

Liu et al., prepared materials of the type $LaMeO_x$ (Me= Zn, Co, and Fe) supported on SBA-15. They analyzed their performance in the $H_2S$ removal. The results showed that the hexagonal arrangement of SBA-15 was not wrecked. They tested in eight successive sulfidation cycles, in which the materials $LaFeO_3$/SBA-15 exhibited better performance and stability in $H_2S$ than $La_2ZnO_4$ and $La_2CoO_4$ supported on SBA-15.[73] This experiment concluded that $LaFeO_3$ did not destroy the arrangement of mesoporous materials.

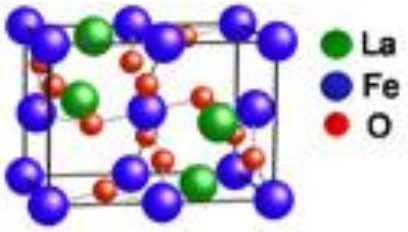


**Figure 15.** Schematic drawing of the crystal structure of perovskite $LaFeO_3$

### 2.8.2. Bismuth Ferrite ($BiFeO_3$)

$BiFeO_3$ is an attractive rhombohedral perovskite material because of its multiferroic antiferromagnetic properties (Figure 16).[74] It is getting a lot of attention due to its narrow bandgap and photocatalytic activity under visible light.[75] The bandgap of $BiFeO_3$ is around 3.00 eV for crystals and 2.67 eV in thin films. It is in the visible region making it promising to harvest the solar energy. The band gap has been shown to be influenced by the size and morphology of the crystals in individual cases.[76,77]

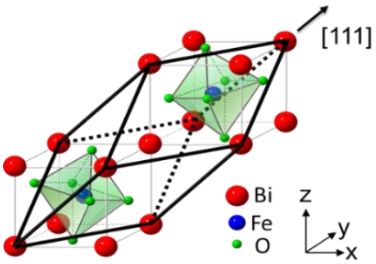


**Figure 16.** Schematic drawing of the crystal structure of perovskite $BiFeO_3$.[78]

Gao et al. designed a $BiFeO_3$ photocatalyst by sol-gel method with a tunable size and a suitable bandgap. This material was used in the degradation of methyl orange (MO) under visible light. It showed a high visible light response due to the small bandgap (2.1 eV). It was concluded that the particle size of $BiFeO_3$ might be the primary factor influencing the photocatalytic efficiency and the light response, although more research is necessary to improve the $BiFeO_3$ photocatalytic performance.[75]

### 2.8.3. Aluminium Ferrite ($AlFeO_3$)

$AlFeO_3$ is an orthorhombic type perovskite material, which retains collinear ferromagnetic structure.[79] This perovskite also offers the advantage of magnetic recovery of the particles which are useful in practical applications. The lattice parameters of $AlFeO_3$ are a= 4.909 Å and c= 13.393 Å.

### 2.8.4. Yttrium Ferrite ($YFeO_3$)

$YFeO_3$ is an orthoferrite material with a distorted perovskite structure. $YFeO_3$ is thermodynamically unstable at high temperatures which makes the synthesis of pure perovskite a challenging task.[80] This perovskite has been widely studied for its magnetic and magneto-optical properties and used in the gas sensor, environmental applications, and catalysis, this material is illustrated in Figure 17.

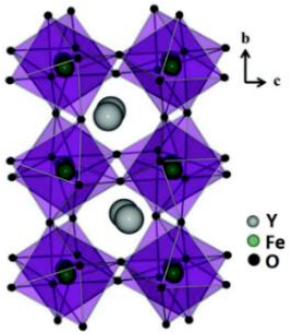


**Figure 17.** Schematic drawing of the crystal structure of perovskite $YFeO_3$.[81]

Diez-Garcia et al. examined the behavior of $YFeO_3$ thin films under illumination. They reported two methods consisting of a deposition of nanoparticles synthesized by ionic liquid route and spin coating of a sol-gel precursor. Both approaches created highly textured films with an orthorhombic phase and direct bandgap transition at 2.45 eV. XPS confirmed a $Fe^{3+}$ oxidation state in both films with a surface composition of 70:30 Y: Fe. Both materials exhibited a response to light, producing hydrogen in alkaline solutions with a potential of 1.05 V.[82] This behavior confirms the use of $YFeO_3$ for photoreduction due to its bandgap and excellent answer under illumination.

### 2.9. $CO_2$ reaction

#### 2.9.1. Adsorption and activation of $CO_2$

The study of the adsorption and activation of $CO_2$ is the primary step for improving the efficiency of $CO_2$ reduction.[83]

Xin Li et al. studied the adsorption of $CO_2$ on heterostructure CdS ($Bi_2S_3$)/$TiO_2$ nanotubes (TNT) photocatalysts.[84] CdS and $Bi_2S_3$ were used as sensitizers and applied to modify TNT photocatalyst. This research indicated that $Bi_2S_3$ and CdS modification can decrease the surface area and the amount absorbed of $CO_2$, but significantly increase the visible light absorption capability and the photocatalytic activity of TNT. Moreover, the amounts adsorbed of $CO_2$ on TNT-$Bi_2S_3$ are higher than those of TNT-CdS.

After the surface modification, the adsorption capacities of the modified TNT for $CO_2$ were decreased. It is also worth noticing that the higher adsorption capacity of $CO_2$ is nearly in

agreement with the increase of surface area of the sample. This concluded that the surface area plays a crucial role in the enhancement of $CO_2$ adsorption. $CO_2$ adsorption ability and charge carrier separation improves when the surface area increases and it leads to the formation of partially charged species. This phenomenon happens through interaction with surface atoms where the high surface area is suitable for capturing small $CO_2$ or $H_2O$ molecules in their cavities. This effect facilitates the $CO_2$ adsorption that leads to the formation of charged species $CO_2^{\delta\bullet}$ with interactions with the surface.[57]

The role of the mesoporous silica is a very important material because it is applied as adsorbent and support. The molecular properties of silica are strongly affected by the nature of their surface sites.

### 2.9.2. $CO_2$ adsorption mode

Adsorption is not only a very important industrial process but also a powerful methodology for the characterization of the surface of materials. The study of the interaction of carbon dioxide with the surface of a group of well-characterized porous, amorphous, ordered, and crystalline silica.[85]

Metal complexes, metal oxides, and silica support are known to activate $CO_2$ and form a variety of activated $CO_2$ complexes.[86] $CO_2$ exhibits different types of coordination modes on the surface of the catalyst (oxygen and carbon coordination). Figure 18 shows the different ways that the $CO_2$ can be adsorbed.

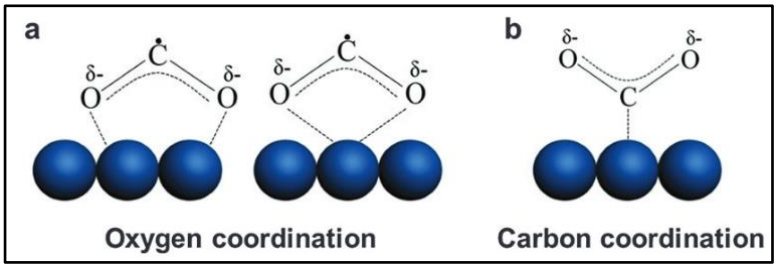


**Figure 18.** The structures of adsorbed $CO_2$ on catalysts.

$CO_2$ is activated trough carbon type coordination on organo-functionalized SBA-15 materials. These carbonite species react with adsorbed water or surface hydroxy groups forming product carbonates, bicarbonates or formats. In the carbon coordination mode, the anchoring of the carbon atom in the $CO_2$ molecule on the silica surface makes difficult the hydrogenation. A hydrogen atom attacks one oxygen in the absorbed molecule to form a carboxyl species (●COOH). [87] This attachment is more favored when $CO_2$ is bound to the surface by the carbon atom because the cleavage of the C-O occurs first. The adsorbed CO can efficiently desorb from the surface of the catalyst with a weak $CO_2$ adsorption.[88]

The adsorbed CO can accept additional electrons to form carbon radicals and subsequently mix with up to four H radicals If the catalyst has a moderate adsorption strength.[89] The adsorbed CO can be hydrogenated to form various hydrocarbon products, the equations of this mode are presented below.

(a) $\bullet O = C = O_{ads} - + H^+ \rightarrow \bullet COOH_{ads}$

(b) $\bullet COOH_{ads} + e^- \rightarrow CO_{ads} + OH^-$.

### 2.9.3. Surface defects

It is widely accepted that the surface defects of nanocatalysts serving as an active site play a decisive role in the adsorption and reactivity of catalytic reactions. The formation of abundant and specific defect sites on the surface of supported nanocatalysts is a promising approach for tailoring the surface morphology and electronic structure to enhance catalytic activity.

Abundant surface vacancy clusters serve as active sites. The silica support with surface defects has been reported by Azsis et al.[90] The high activity of Ti/SBA-15 is due to the presence of both intra- and interparticle porosity which led to a high concentration of basic sites and oxygen vacancy sites. The presence of defect sites and oxygen vacancies in MSN (mesostructured silica nanoparticles) is responsible for the formation of surface carbon species, while Ti sites dissociated hydrogen form atomic hydrogen. The surface carbon species then interacted with an atomic hydrogen to form methane.

The nature of the support plays a crucial role in the high activity of $CO_2$. Single metal oxides and mesoporous materials possess different characteristic and show good potential to be used as supports for Ti catalyst.

### 2.9.4. Reaction mechanism

Although the $CO_2$ reaction is a simple reaction, its mechanism appeared to be difficult to establish. Presently, there are still arguments on the nature of the intermediate compound involved in the process and on the methane formation scheme.

Firstly, $CO_2$ and $H_2$ are absorbed onto metal sites, followed by dissociation to form CO, O and H atoms, and migration onto the MSN surface.[91] The CO then interacted with oxide surfaces of the MSN to form bridged carbonyl and linear carbonyl. Bidentate formate was also formed through the interaction with atomic hydrogen. Meanwhile, the O atom split over onto the surface of the MSN and was stabilized in the oxygen vacancy site near the metal site. The adsorbed oxygen then reacted with atomic hydrogen to form hydroxyl on the MSN surface in which a further reaction with another atomic hydrogen formed a water molecule.

Finally, the adsorbed carbon species was further hydrogenated to methane and another water molecule.[92] The proposed mechanism process is illustrated in Figure 19. The oxygen vacancies can serve as reactive surface sites because the $CO_2$ species are generated as result of electron gain by $CO_2$. The regeneration of oxygen vacancies in the photocatalysts is therefore still a problem that needs to be solved.[93]

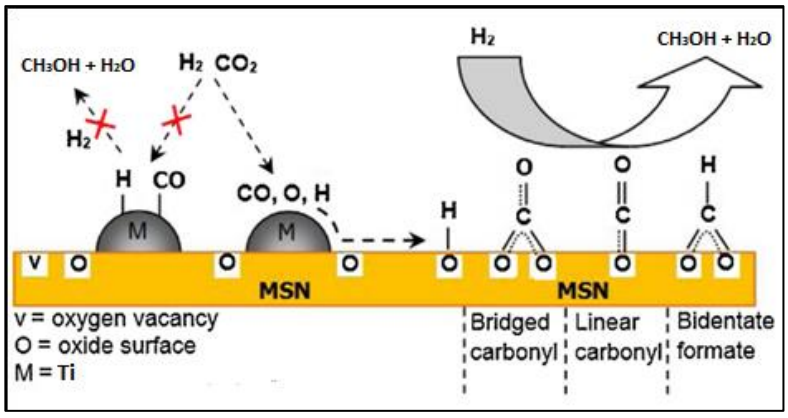


**Figure 19**. Dissociation of $CO_2$ supplies an oxygen atom.[94]

### 2.9.5. Conditions of $CO_2$ reaction

The two typical reaction modes that have been utilized for the photocatalytic reduction of $CO_2$ with $H_2O$ are solid-liquid and solid-vapor. In the solid-liquid mode, the photocatalyst is immersed in an aqueous solution where $CO_2$ and the solid-liquid phase interacts occurring the photoreaction. But, there are several problems related to the interaction between $CO_2$ and $H_2O$ in the liquid phase such as the low solubility of $CO_2$ in $H_2O$. In the solid-gas interaction, the catalyst is surrounded by $CO_2$ and $H_2O$ vapor.[95]

The main differences between the two modes are when the photogenerated electrons are created, this $e^-$ are used for the reduction of $H_2O$ to $H_2$ in solid-liquid phase. While in the solid-gas mode, the same electrons allow the exposure of the catalyst surface to $CO_2$ and reduce the formation of $H_2$. The conclusion is that the solid-gas phase is preferably in the reduction of $CO_2$. The reaction modes can be illustrated in Figure 20.

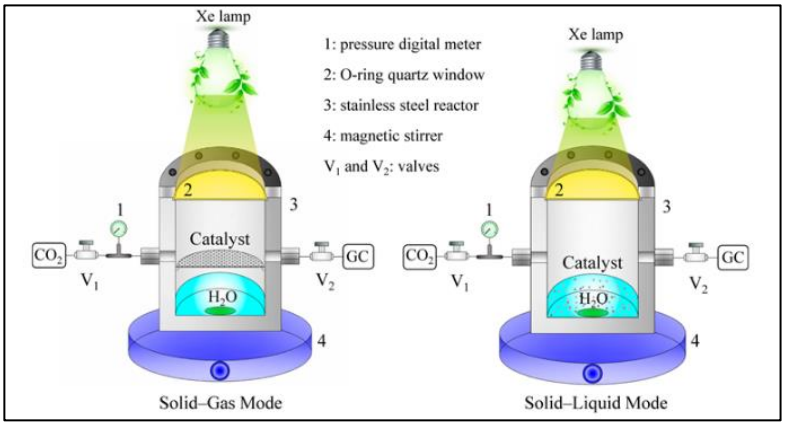


**Figure 20.** Reactor for photocatalytic reduction of $CO_2$ with $H_2O$. a) solid-gas mode, b) solid-liquid mode.[96]

Xie et al. tested the implementation of a reaction mode based on solid-vapor. They found that the use of this type of reaction mode increased the selectivity of photogenerated electrons in the reduction of $CO_2$ to CO in comparison with the solid-liquid system.[96] The primary factor was the reduction of $H_2O$ to $H_2$ first than carbon fuels. This research confirms that the water acts as an electron donor in the system and also the solid-vapor system is better in comparison with the traditional method.

## 2.10. Summary

The aim of this chapter is to know the photocatalytic reduction of carbon dioxide ($CO_2$) as a generate valuable chemical method by artificial catalysts to obtain solar fuels such as methane, due to the increasing $CO_2$ emissions and the shortage of the fossil resources. An efficient $CO_2$ photoreduction catalysis involves the combination of catalysts, semiconductor such as $TiO_2$, and perovskites. $TiO_2$ is the golden material due to its special characteristics such as a large surface area and strong adsorption ability.

To prevent the recombination of e- and h+ pairs mesoporous network structures such Ti incorporated SBA and KIT series was reported to enhance the adsorption of the reactive species and utilization of the incident light and thereby increase the photocatalytic activity. The photoreduction of $CO_2$ over $TiO_2$ via the confined space effect of the ordered mesoporous structure not only shows a higher production efficiency of $CH_3OH$ than the commercial $TiO_2$ but also exhibits better stability for $CO_2$ photoreduction.

SBA-15 and KIT-6 have been chosen as support due to their main characteristics such as surface areas and large in pore sizes. The beneficial study of the synthesis of the silica supports helps to know the optimal conditions (temperature, time of calcination, steps) to have a good surface area and large pore sizes. This study and analysis were described in the section 2.6.3.

The perovskite metal oxides have aroused as promising photocatalyst materials to operate $CO_2$ transformation reactions because of their stable crystal structure, and high catalytic activity. The ferrite perovskite material has its native bandgap in the visible region (3.2 eV), so it is necessary to expand its position to the corresponding reduction potential to get the desired products ($CH_3OH$). One of the methods that I studied in this work to expand the bandgap of the semiconductor is to confined in the mesoporous material. Herein, I demonstrated the facile synthesis of the silica support, ferrite perovskites, and characterization by various techniques (e.g. $N_2$ adsorption-desorption, XRD, and Uv-Vis). And finally, the study of the reaction mechanism and pathways of $CO_2$ reduction, as well as their dependent factors are also analyzed and discussed. This is expected to increase the efficiency of the reduction through controlling the selectivity towards the $CH_3OH$ product.

The work done in Eslava group has been: (i) synthesis of SBA-15 and KIT-6 through the hydrothermal method and analyzed by $N_2$ adsorption-desorption, XRD, and UV-Vis measurement, (ii) Semiconductors ($TiO_2$, $LaFeO_3$, $BiFeO_3$, $AlFeO_3$, and $YFeO_3$) synthesized by sol-gel route and analyzed with the same methods as silica supports, and (iii) Synthesis and study of confined photocatalysts in the mesoporous silica support at different loadings.

# 3. EXPERIMENTAL METHODOLOGY

## 3.1. Materials

The material utilized in this project are:

- Pluronic 123 ([poly (ethylene oxide)-block- poly (propylene oxide)-block- poly (ethylene oxide)], ($EO_{20}$-$PO_{70}$-$EO_{20}$, Aldrich)
- Tetraethyl orthosilicate (99.99% trace metal basis, sigma Aldrich)
- 1-butanol (99.4%, Sigma Aldrich)
- Titanium (IV) isopropoxide (97%, sigma Aldrich)
- 2-Propanol (anhydrous 99.5%, sigma Aldrich).
- Lanthanum (III) nitrate hexahydrate (La $(NO_3)_3 \cdot 6H_2O$), sigma Aldrich
- Iron (III) nitrate nonahydrate (Fe $(NO_3)_3 \cdot 9H_2O$), sigma Aldrich

## 3.2. Photocatalytic supports

### 3.2.1. SBA-15

SBA-15 was synthesized by the hydrothermal method proposed by Zhao et al.[97] Pluronic 123 surfactant was dissolved (4 g) in an HCl 2M solution (8.75 g) and distilled water (120 g) and vigorously stirred for 4 h at 35°C. Then, 8.6 g of TEOS (Tetraethylorthosilicate) was added as the silica source, and the solution was kept under stirring for 24 h at 35°C. After that, the material obtained was transferred to a Teflon-lined autoclave and heated at 90°C for 24 h. The product was recovered by filtration, dried at 80°C. To remove P123 and liberate the silica pores, heat treatment was performed in air in an oven at 550°C for 6h with a rate of 2°C/min for surfactant template removal.

### 3.2.2. KIT-6

KIT-6 was synthesized following the process proposed by Kleitz et al.[98] 6g of Pluronic 123 was dissolved in 11.9g of HCl 0.75 M solution and 217 g of distilled water. To this, 6 g of 1-butanol was added under vigorous stirring at 35°C. After 1 h stirring, 9 g of TEOS was added dropwise, and after another hour 3.9 g of TEOS was poured. The mixture was left under stirring at 35°C for 24 h and subsequently heated for 24 h in a Teflon-lined autoclave at 100°C.

The product obtained after the hydrothermal treatment immediately was filtered without washing and dried at 100°C overnight. Finally, the template was removed by extraction with an ethanol-HCl mixture, and it was calcined at 550°C for 9 h for surfactant template removal.

### 3.3 Semiconductors

#### 3.3.1. $TiO_2$

The semiconductor $TiO_2$ was synthesized following the procedure by Yang et al.[35] Titanium IV isopropoxide (TTIP) was added dropwise in 2-Propanol (volume ratio TTIP: 2-propanol of 1:8). Water was slowly added to the resulting solution to cause the hydrolysis of the TTIP (TTIP: water volumetric ratio of 1:10). The stirring was maintained for 2 h to hydrolyze TTIP completely. The material was recovered by centrifugation with a mixture of ethanol and deionized water. In the end, the solution was dried at 80°C overnight and calcined at 700°C for 2 h.

#### 3.3.2. $LaFeO_3$

$LaFeO_3$ was synthesized as follows.[70] La $(NO_3)_3 \cdot 6H_2O$ and Fe $(NO_3)_3 \cdot 9H_2O$ were dissolved in equimolar amounts (0.005 mol) with citric acid (0.010 mol) in a 25 ml $H_2O$ and ethanol mixture ($H_2O$: ethanol 1:2) to yield a homogeneous solution. The solution was stirred for 10 min, sonicated for another 10 min at room temperature, and finally heated in a bath at 70° C until evaporation. The resulting gel from the evaporation was dried at 90°C for 24 h in an oven and calcined at 600°C (with a heating rate of 2 °C/min) for 5h.

#### 3.3.3. $BiFeO_3$

The $BiFeO_3$ powder was synthesized by a simple sol-gel route.[75] 0.005 mol of Bi $(NO_3)_3 \cdot 5H_2O$ and Fe $(NO_3)_3 \cdot 9H_2O$ were dissolved in stoichiometric proportions (1:1 molar ratio) in 50 ml of ethylene glycol (0.4 M) as the precursor solution. The mixture was stirred for 90 min at 80°C to obtain a viscous gel (sol). Next, it was kept at 120°C for 3 days to form a xerogel powder. Then, the powder was first calcined at 300°C for 4 h as a pre-treatment and finally at 600°C for 2 h.

### 3.3.4. $AlFeO_3$

$AlFeO_3$ was synthesized as follows.[99] 0.005 mol of Al $(NO_3)_3 \cdot 9H_2O$ and Fe $(NO_3)_3 \cdot 9H_2O$ were dissolved in stoichiometric proportions (1:1 molar ratio) in 20 ml of distilled water. 10 ml $NH_4OH$ (25% concentration) was added dropwise to the mixture until the appearance of a dark red solution, showing the formation of iron hydroxide. The solution was kept under stirring for one hour, and a small amount of acetone was added to allow the reaction to precipitate. Next, the liquid was maintained at 70°C in a bath until evaporation. The gel was dried at 80°C overnight and calcined at 700°C for 1 h.

### 3.3.5. $YFeO_3$

$YFeO_3$ was synthesized under hydrothermal conditions as follows.[100] 0.005 mol of $Y(NO_3)_3 \cdot 6H_2O$ and $Fe(NO_3)_3 \cdot 9H_2O$ were dissolved in stoichiometric proportions (1:1 molar ratio) in 30 ml distilled water under stirring. Next, 30 g of solid NaOH as a mineralizing agent was added to the solution. Next, the mixture was transferred to a Teflon-lined autoclave where the crystallization was performed at 240°C for 72 h. The dark product was filtered several times with distilled water to obtain crystals and dried at 80°C overnight in air.

## 3.4. Synthesis of $SiO_2$-Semiconductors

### 3.4.1. $SiO_2$-$TiO_2$

The $TiO_2/SiO_2$ materials were prepared by hydrolysis of titanium IV isopropoxide into the silica support (KIT-6 or SBA-15) via sol-gel method following the procedure by Yang et al.[35] The silica material was sonicated in isopropanol. Then, the required amount of TTIP was added dropwise to the solution under stirring for 45 min. Water was then slowly added (TTIP: water with volumetric ratio 1:10) to cause the hydrolysis of TTIP, and the solution was stirred at room temperature for 2 h. The material was recovered by centrifugation with deionized water and ethanol, dried at 80°C and calcined at 700 °C for 2h.

### 3.4.2. $MFeO_3$-$SiO_2$ (where M= La, Bi, Al, and Y)

$MFeO_3/SiO_2$ materials were synthesized following the process proposed by Liu et al.[73] We take the preparation of $LaFeO_3/SiO_2$ as an example. 0.01 mol of La $(NO_3).6H_2O$ and 0.01 mol of $Fe(NO_3).9H_2O$ were dissolved in 4.5 ml of deionized water, Then, drops of $HNO_3$ (6M,

previously prepared) were poured until the solution changed color to avoid hydrolysis. Afterward, citric acid was added (citric acid/Fe= 1.5 molar ratio).

Then, 0.25 g of the synthesized silica support was added to the mixture. The solution was kept at 60 °C over a water bath under stirring until a viscous gel was formed. The gel was aged at room temperature for three days and dried at 80 °C overnight, and finally, it was calcined at 550 °C for 6 h. Similar procedure was realized with the preparation of $BiFeO_3/SiO_2$, $YFeO_3/SiO_2$, and $AlFeO_3/SiO_2$.

The theoretical weight of silica and M (M= La, Bi, Al, and Y) supported catalyst was controlled to be 5%, 10%, and 20% respectively. For comparison, pure semiconductor without the addition of $SiO_2$ powders was prepared using the methods above, which can be defined as weight= 0%.[101]

### 3.5. Characterization

#### 3.5.1. X-Ray Diffraction (XRD)

The supports, catalysts, and perovskites were characterized by XRD using a Brucker D8-Advance and Cu Kα radiation with a wavelength of 1.5418 Å, with a continuous scan of 0.6° $min^{-1}$ without rotation in the ranges $1.0° < 2\theta < 5°$ and $30° < 2\theta < 80°$ with a constant scan rate.

The crystallite sizes were calculated from the Scherrer equation (Equation 1).[102]

$$D = \frac{0.9\lambda}{\beta \cos\theta} \qquad (1)$$

Where λ is the wavelength of the X-rays, θ is the diffraction angle, and β is the corrected full width at half-maximum (FWHM) calculated by OriginPro.

#### 3.5.2. Nitrogen adsorption-desorption

The textural properties (specific surface area, pore volume, and pore diameter distribution) of the catalysts were determined from nitrogen isotherms measured using a Micromeritics 3Flex. The specific surface area was calculated by the Brunauer-Emmett-Teller (BET) equation, while

the pore diameter distribution and pore volume were determined using Barrett-Joyner-Halenda (BJH) method. Before the physisorption of $N_2$, the samples were degassed at 350°C for 2h.

Wall thickness (δ) was calculated (Equation 2) from the difference between the lattice parameter (hexagonal array) and pore diameter.[103]

$$\delta = a_o - D_p \qquad (2)$$

$$a_o = \frac{2d_{100}}{\sqrt{3}} \qquad (3)$$

Where $a_o$ is the cell parameter (hexagonal array) (Å), $d_{100}$ is the inter-planar distance (from Scherrer's equation), d= λ/2 sin (θ), λ is the X-rays wavelength (Å), θ is the diffraction angle, δ is the wall thickness (Å) and $D_p$ is the pore diameter (from BJH calculations, $N_2$ physisorption isotherm) (Å).

### 3.5.3. UV-visible spectroscopy (UV-vis DRS)

The catalysts were characterized by UV-Vis spectroscopy in a Perkin Elmer Lambda 40 equipped with an integrating sphere. The reflectance data was processed using the Kubelka-Munk function (F (R∞)), Equation 4, in which R∞ is the reflectance at infinite depth.

$$F(R_\infty) = \frac{(1-R_\infty)}{2R_\infty} \qquad (4)$$

The band edge position of the semiconductor at the point zero charge can be calculated using the following empirical equations: [102]

$$E_{VB} = X - E^e + 0.5E_g \qquad (5)$$

$$E_{CB} = E_{VB} - E_g \qquad (6)$$

Where $E_{VB}$ represents the valence band (VB) edge potential, X is the electronegativity of the semiconductor, $E^e$ is the energy of free electrons on the hydrogen scale (~4.5 eV), $E_{CB}$ is the conduction band (CB), and $E_g$ is the band gap of the semiconductor.

A method to estimate the electronegativity was developed by Robert Mulliken with the use of the values of the first ionization energy (IE) and the electron affinity (EA) to calculate the electronegativity of the semiconductors. The values are: $LaFeO_3$- 5.54 eV, $BiFeO_3$- 5.89 eV, $YFeO_3$- 5.63 eV, $AlFeO_3$- 5.61 eV and $TiO_2$-5.81 eV. The purpose of this is to find the band edges and the possible products according to their redox potentials.[104]

# 4. RESULTS AND DISCUSSION

## 4.1. Photocatalytic support

The results of the characterization techniques performed on the SBA-15 and KIT-6 supports are presented in the following sections.

### 4.1.1. X-Ray Diffraction (XRD)

Small angle X-ray diffraction (SAXS) patterns were measured on SBA-15 and KIT-6. SBA-15 presented an intense sharp peak which can be indexed as $d_{100}$ spacing and two well-resolved peaks indexed as $d_{110}$ and $d_{200}$ spacings (Figure 21-A). The $d_{100}$ reflection is distinctive of the SBA-15 mesoporous material structure; the $d_{110}$ indicates the 2D pore system, and the $d_{200}$ indicates the periodicity of the pore system. The presence of the three distinct Bragg diffractions confirms a 2D hexagonal lattice with p6mm symmetry arrangement of mesopores and high crystallinity according to JCPDS card no. 744-1394.[105–107]

The KIT-6 pattern showed a sharp and intense peak at $2\theta=1.06°$ corresponding to $d_{211}$ reflexion and two weak peaks indexed as $d_{220}$ and $d_{420}$ (Figure 21-B). These peaks indicate that the material is well ordered and belongs to continuous cubic space group $la_3d$, according to JCPDS card no. 744-1394.[37]

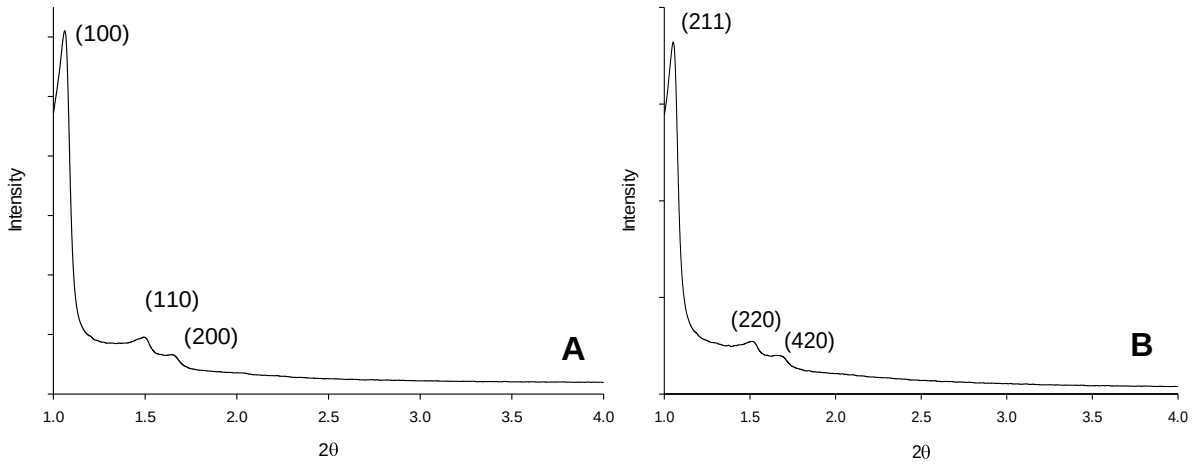


**Figure 21.** Small- angle XRD patterns of (A) SBA-15 and (B) KIT-6.

The wide-angle XRD patterns of the silica supports are shown in Figure 41, Appendix 7.1. The patterns revealed no defined diffraction, indicating the amorphous nature of the $SiO_2$ walls. There is only one broad peak at a 2θ value of 20-30° characteristic of silicas.[108]

### 4.1.2. $N_2$ adsorption-desorption

In Figure 22, the supports SBA-15 and KIT-6 showed a shape of isotherm that is classifiable as type IV and hysteresis H1 loop according to IUPAC. This type of isotherm is characteristic of the mesoporous materials with pores with a constant cross-section (cylindrical).[109] The isotherm presented an inflection at P/Po= 0.6-0.85 presenting a near-equilibrium desorption that corresponds to the existence of mesopores with a narrow pore size distribution. Hysteresis loop H1 occurs when the adsorption and desorption branches are vertical with a parallel design, distinctive for uniform cylindrical pores.[110]

The three-dimensional KIT-6 pore system presented narrower hysteresis loop in comparison to the 2D SBA-15. The interconnected 3D network of channel pores (KIT-6) is smaller than the independent mesopore system with cylindrical channels in SBA-15.[111]

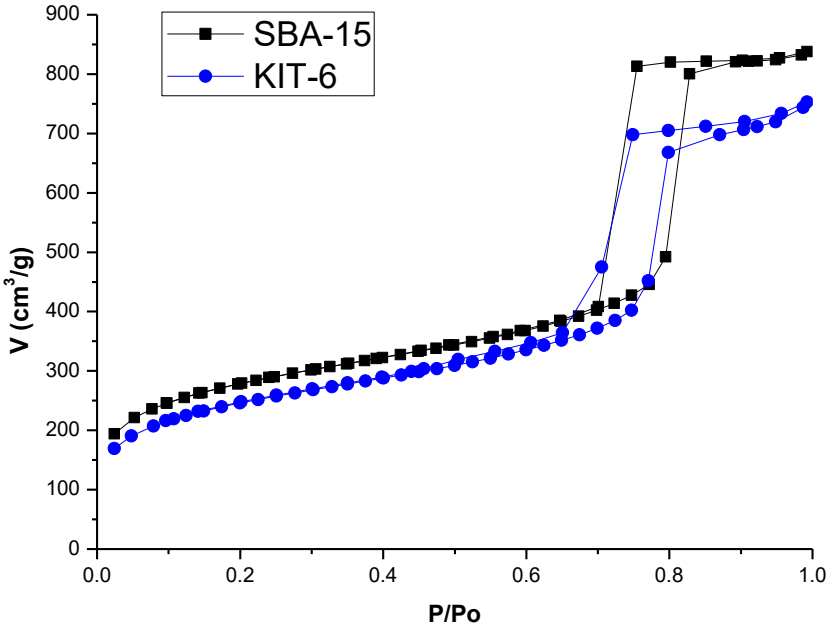


**Figure 22.** $N_2$ adsorption-desorption isotherms of support SBA-15 and KIT-6.

Pore size distribution of KIT-6 and SBA-15 (Fig 23) confirmed that the adsorption and desorption have a well-defined pore size diameter with a pore size centered at 8 nm measured during desorption, at meniscus equilibrium conditions.[112,113]

Both materials are known to have a secondary pore system in their walls (intrawall pores), with sizes in the micropore range.[105] The presence of intrawall pores explains the large surface areas measured, with values of 933 and 833 $m^2/g$ for SBA-15 and KIT-6, respectively.[114] The low amount pores detected in KIT-6 (~4 nm) must result from cavitation effects, that is, from the sudden nucleation of nitrogen in ink-bottle pores with narrow necks in the material. Their amount is negligible compared to the abundance of the 8 nm pores.[115,116]

There is a strong relationship between the adsorption and desorption pore size distribution. The adsorption pore size distribution corresponds to a progressive filling of mesopores, whereas desorption generally leads to a sudden emptying of the same pores. As a consequence, the desorption branch gives a narrower pore size distribution than the adsorption branch. This is the reason that the desorption branch is the parameter reported in table 2 as true pore size. But others authors claim that the adsorption branch should be used instead, as it gives the complete pore size distribution and not the size of the necks from which the condensed gas could quickly be evacuated upon desorption.[117]

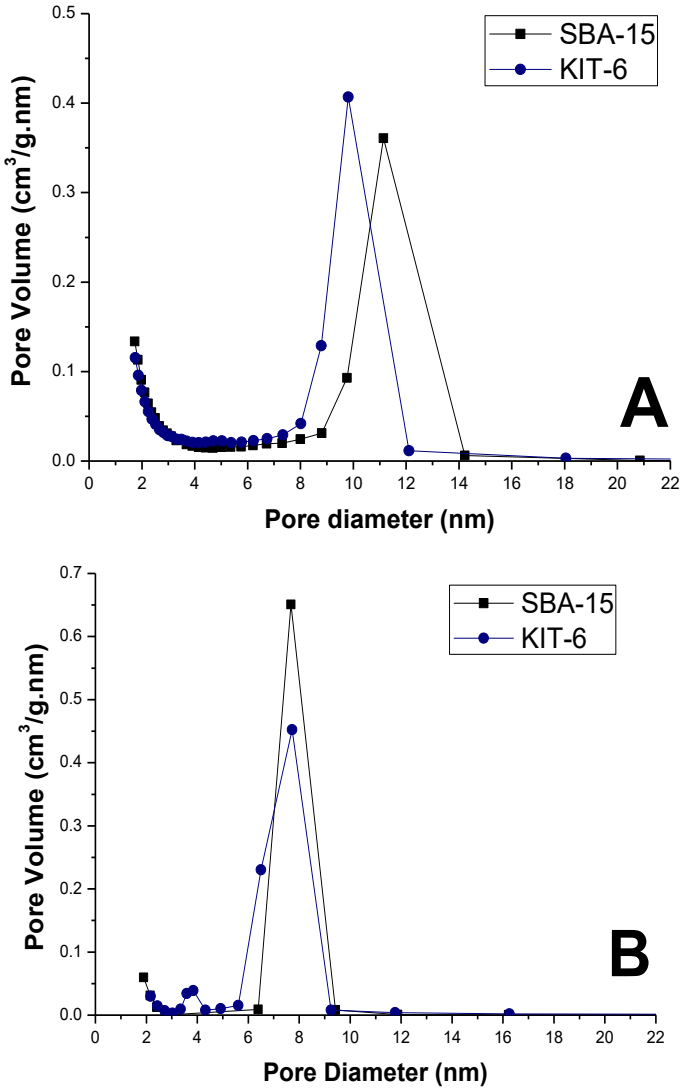


**Figure 23.** Pore size distribution of SBA-15 and KIT-6 (A) adsorption (B) desorption

Textural properties obtained from the 3Flex™ are presented in Table 2 in which SBA-15 and KIT-6 have shown a large specific surface area and pore volume. The main differences between these materials are their pore sizes and the structure connectivity for SBA-15 (2D) and KIT-6 (3D) pore structure.[118] The large pore wall thickness (δ) was calculated with the information of $d_{100}$ spacing and pore diameter.[119]

**Table 2.** Textural properties of SBA-15 and KIT-6 supports

| **Supports** | **$S_{BET}$ ($m^2/g$)** | **$D_p$ (nm)** | **$V_t$ ($cm^3/g$)** | **$a_o$** | **δ (nm)** |
|---|---|---|---|---|---|
| **SBA-15** | 933 | 7.7 | 1.12 | 8.9 | 1.6 |
| **KIT-6** | 833 | 7.7 | 1.03 | 18.9 | 2.4 |

Where: $S_{BET}$: BET surface area, $D_p$= pore diameter, $V_t$= total pore volume, $a_o$= unit cell parameter estimated from the XRD. Equations 2 and 3 (see Experimental section).[120]

To summarise, SBA-15 and KIT-6 were successfully synthesized with pore diameters around 8 nm, high specific surface area, and cylindrical pores. These characteristics make the supports good candidates to be a host of metal oxides species, and their pore diameter is suitable to allow the $CO_2$ molecule to be adsorbed with no problem ($CO_2$ size=3.4 Å).[121]

## 4.2. Semiconductors

### 4.2.1. $N_2$ adsorption-desorption

The information about the specific surface area ($S_{BET}$) and pore volumes of all the materials prepared are listed in Table 3. SBA-15 and KIT-6 decreased their specific surface areas significantly with a load of photocatalysts (up to 50-75%), indicating that there was deposition of the photocatalysts on the silica supports.

Comparison between the results obtained for SBA-15 and KIT-6 indicate that they behave differently as supports for $TiO_2$. KIT-6 incorporates much less $TiO_2$ than SBA-15. The differences could be attributed to the differences in mesopore structure shape, KIT-6 comprising a three-dimensional pore structure, which can affect how Ti precursors diffuse and react with the silica surfaces.[122]

The deposition of $LaFeO_3$, $BiFeO_3$, $AlFeO_3$, and $YFeO_3$ on both KIT-6 and SBA-15 seems quite consistent for both silica supports since the specific surface area decreased similarly for both cases. The results of surface area and pore volume verified that the perovskites were deposited on the silica supports. Whether this deposition was inside the pore channels or on the external surface of the silica particles requires analysis of the pore size distribution curves.[123]

**Table 3.** Textural properties of semiconductors with SBA-15 as support

| Sample | SBA-15 | | | KIT-6 | | |
|---|---|---|---|---|---|---|
| | $S_{BET}$ ($m^2/g$) | $D_p$ (nm) | $V_t$ ($cm^3/g$) | $S_{BET}$ ($m^2/g$) | $D_p$ (nm) | $V_t$ ($cm^3/g$) |
| **$TiO_2$ (20%)** | 281 | 7.6 | 0.42 | 483 | 6.6 | 0.52 |
| **$TiO_2$ (10%)** | 455 | 7.6 | 0.58 | 641 | 6.5 | 0.75 |
| **$TiO_2$ (5%)** | 727 | 6.5 | 1.10 | 733 | 5.4 | 0.77 |
| **$LaFeO_3$ (20%)** | 201 | 3.3 | 0.18 | 238 | 3.6 | 0.18 |
| **$LaFeO_3$ (10%)** | 429 | 4.9 | 0.52 | 379 | 3.7 | 0.38 |
| **$LaFeO_3$ (5%)** | 507 | 7.7 | 0.72 | 493 | 7.2 | 0.68 |
| **$BiFeO_3$ (20%)** | 238 | 3.5 | 0.19 | 187 | 5.5 | 0.20 |
| **$BiFeO_3$ (10%)** | 274 | 5.5 | 0.32 | 320 | 6.5 | 0.50 |
| **$BiFeO_3$ (5%)** | 378 | 5.5 | 0.41 | 373 | 6.6 | 0.54 |
| **$YFeO_3$ (20%)** | 305 | 4.8 | 0.31 | 365 | 3.8 | 0.22 |
| **$YFeO_3$ (10%)** | 381 | 4.8 | 0.34 | 464 | 6.4 | 0.61 |
| **$YFeO_3$ (5%)** | 521 | 5.6 | 0.51 | 550 | 6.5 | 0.71 |
| **$AlFeO_3$ (20%)** | 361 | 3.8 | 0.37 | 418 | 5.6 | 0.56 |
| **$AlFeO_3$ (10%)** | 488 | 4.3 | 0.51 | 522 | 6.4 | 0.68 |
| **$AlFeO_3$ (5%)** | 577 | 5.5 | 0.56 | 638 | 6.5 | 0.84 |

Where: $S_{BET}$: BET surface area, $D_p$= Pore diameter, $V_t$= total pore volume.

Figures 24-32 present the $N_2$ adsorption-desorption isotherms and pore size distributions of all the materials prepared. The effect in adsorption-desorption isotherms involves a combination of physical mechanics which is reproduced in different types of hysteresis loops giving information about the pore size and shape.

$TiO_2$/SBA-15 samples (Fig 24-A) show sharp capillary condensation around P/Po=0.6-0.9 for all samples containing $TiO_2$, but the maximum amount adsorbed decreases with increasing loading of the precursors. The isotherm shape conservation means that the incorporation of $TiO_2$ into SBA-15 did not destroy the structure of the support. This effect can be attributed to the incorporation of $TiO_2$ in SBA-15 post-synthesis where the titanium species could have reacted with the surface of the walls (silanol groups). As a result, the surface area and pore volume decreased, but the characteristic pore arrangement of SBA-15 was kept.

$TiO_2$/KIT-6 isotherms in Figure 24-B show the same behavior as in SBA-15. There is a sharp capillary condensation around P/Po=0.6-0.8, and the isotherm shape is kept with the loading of $TiO_2$. The amount of nitrogen adsorbed decreases with the amount of $TiO_2$ indicating its loading on the SBA-15. There is also a small kink in the desorption at P/Po= 0.45-0.5, characteristic of nitrogen cavitation. This effect occurs in ink-bottle type pores where the evaporation during the desorption is limited by a hemispherical meniscus in the pore neck, and the pore body remains full until there is a sudden bubble nucleation of the nitrogen, typically occurring at P/Po=0.40.[124]

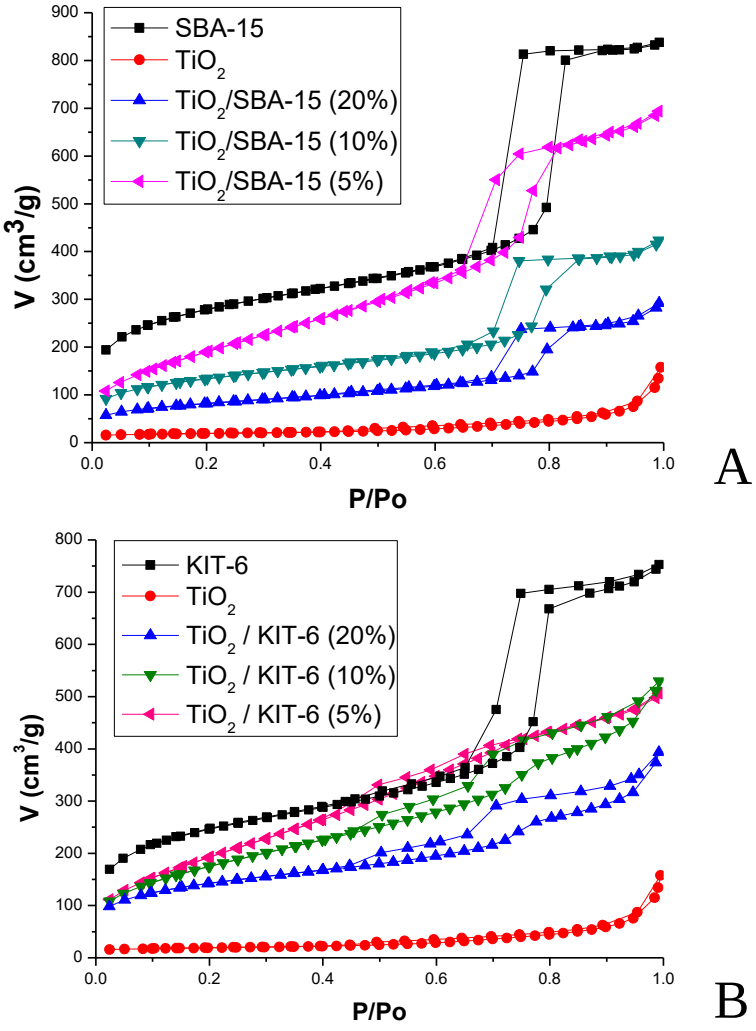


**Figure 24.** Nitrogen adsorption desorption isotherm for $TiO_2$ series catalysts: (A) SBA-15 and (B) KIT-6

The pore size distributions (PSD) of $TiO_2$/SBA-15 samples were calculated on adsorption-desorption isotherms using BJH model (Fig. 25). In complex porosities, the adsorption PSD gives information of the pore body and the desorption PSD of the pore neck. The incorporation

of $TiO_2$ into the support mainly affected the adsorption PSD, indicating a slight shrinkage of the pore body size of 2-3 nm.

However, the desorption showed that most samples have the same pore neck size, except the 5% $TiO_2$/SBA-15 which shrunk 1 nm. These results show that there was an incorporation of $TiO_2$ in the pore network, specifically for the 5% loading which also affects the pore neck size. But for larger loadings, the $TiO_2$ precursors probably agglomerate and precipitate on the surface of the SBA-15 particles as we can deduce in figure 25-B, where the pore diameter persists with no big changes in comparison with SBA-15.[125,126] But at higher amounts of TTIP, the second step of the $N_2$ isotherm remains with no change. This means that the deposition of the extra titania can be located outside the pores or inside closing the pore completely, confirming the results in the pore size distribution.[127]

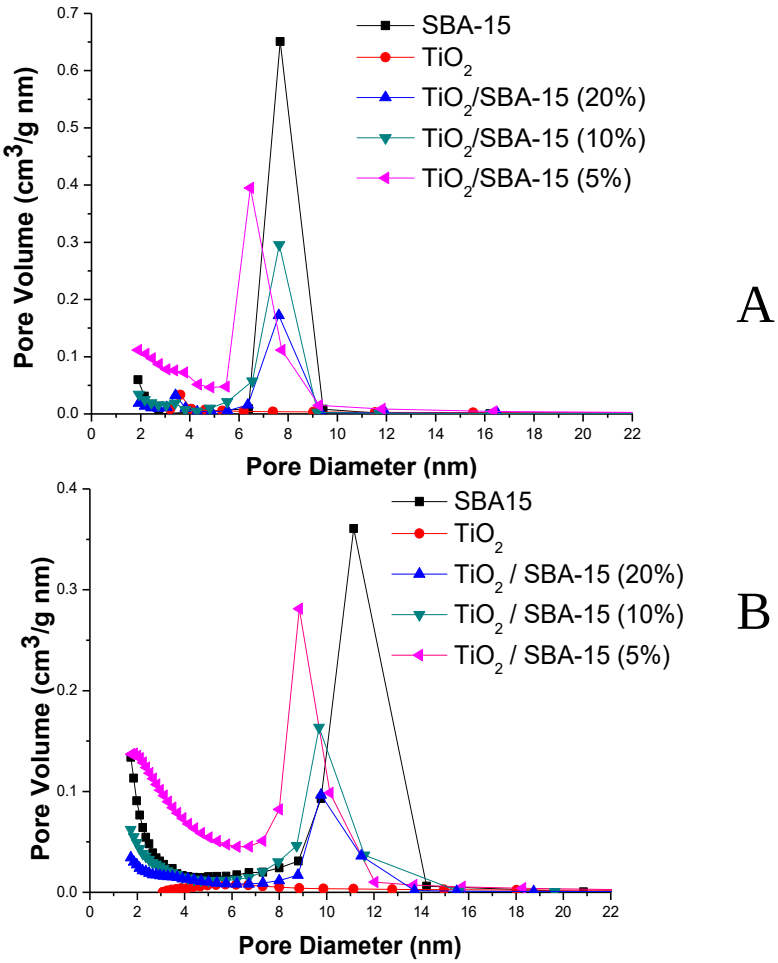


**Figure 25.** Pore size distribution of $TiO_2$ / SBA-15 catalysts: (A) adsorption and (B) desorption.

The PSDs of KIT-6 loaded with $TiO_2$ are shown in Fig 26. The maximum of the PSD curve of KIT-6 calculations using the adsorption branch is shifted to a bimodal distribution. The presence of cavitation indicated the presence of narrow necks (smaller than 4 nm), this may offer gas diffusion limitations for the photocatalytic reactions. The results indicated that the best loading was 5% since this influenced both adsorption and desorption PSD. This is indicative of a better uniformity and dispersion of the load of the precursors leading to a decrease in the pore volume of the main peak (about 8 nm).[128]

Pore diameter from desorption is larger than the pore diameter from adsorption indicating that higher loading can induce agglomeration of species and deposition on the surface of the KIT-6 particles.[129] The 3D pore structure was able to accommodate dispersed $TiO_2$ and facilitate a faster diffusion of the products. Moreover, the PSDs show a bimodal distribution with pore sizes in the range of 2-4 and >5 nm, respectively. It can be speculated to be defects in the ordered structure of the material depending on the degree of incorporation of the precursor. The wider PSDs at the range of 2-8 nm, can be further separated into two kinds of pores: one is about 4 nm and the other at 7 nm. These regions are affected by the adsorption of the $TiO_2$ particles, which caused a decrease of the pore size diameter.[130]

Early reports indicated that KIT-6 is composed by two sets of interpenetrating mesopores, in which each set of mesopores is independent. Recent studies have contradicted this view, suggesting that these sets are interconnected by micropores. If $TiO_2$ is within the pores of KIT-6 can do so across both sets of pores. The result of this is the appearance of a bimodal distribution about 4 nm, and 5-8 nm.[36]

The PSD of KIT-6 features not only the main peak that corresponds to the main mesoporous channel of KIT-6 but also a substantial amount of pores in the range between 2 and 5 nm (intrawall pores). The parts of PSD curves corresponding to intrawall pores show a maximum peak at about 3 nm, this observation indicates that the peak in PSD is real and not an artifact. The pore volume associated with the 3 nm modal peak increases with the increase of content, this means that some precursors are in the intrawall pore.[131]

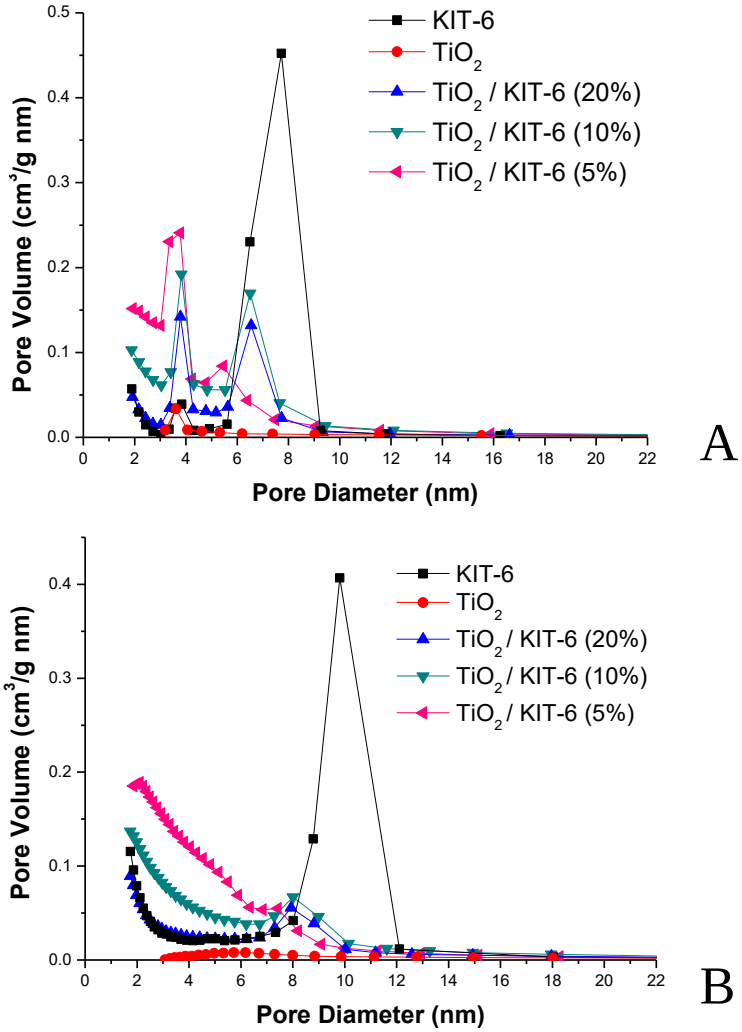


**Figure 26.** Pore size distribution of $TiO_2$/KIT-6 catalysts: (A) adsorption and (B) desorption

The isotherms for $LaFeO_3$ on SBA-15 and KIT-6 are shown in Figure 27. The loading of $LaFeO_3$ is evident since in both cases there is a decrease of the nitrogen adsorbed. It is noted that the hysteresis becomes less upright with increasing loading of $LaFeO_3$, indicating the change in shape of the pore network which must be due to some filling of the pores.[132]

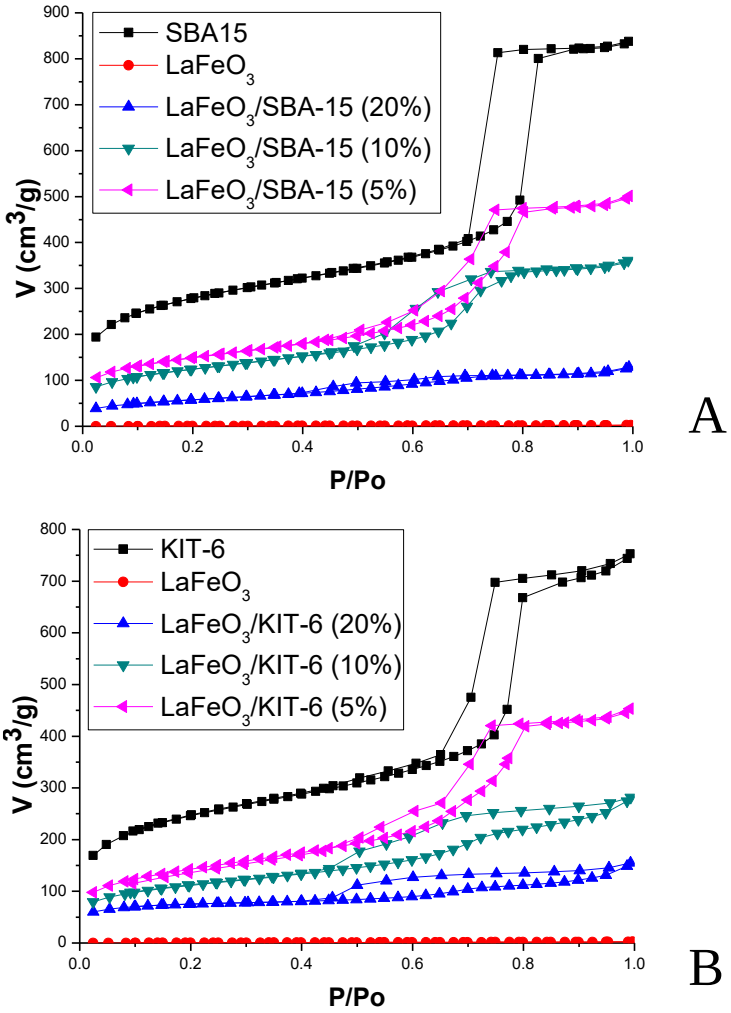


**Figure 27.** Nitrogen adsorption-desorption isotherm for $LaFeO_3$ series catalysts: (A) SBA-15 and (B) KIT-6.

The PSD of $LaFeO_3$/SBA-15 series in Fig 28 shows the shrinkage in pore sizes in all the samples with the loading of $LaFeO_3$. Both pore bodies and necks decrease in size. The higher the loading, the larger the shrinkage. $LaFeO_3$ series for both supports especially for 5% loading became bimodal for the larger pore size.

These results assume that there was a partial transformation of the SBA-15 and KIT-6 pore network leading to a bimodal material with two sets of well-defined pore sizes due to the deposition of the species inside the network. This indicates that the smaller mesopores act as bottlenecks and restrict the accessibility to the larger mesopores of the supports.[133]

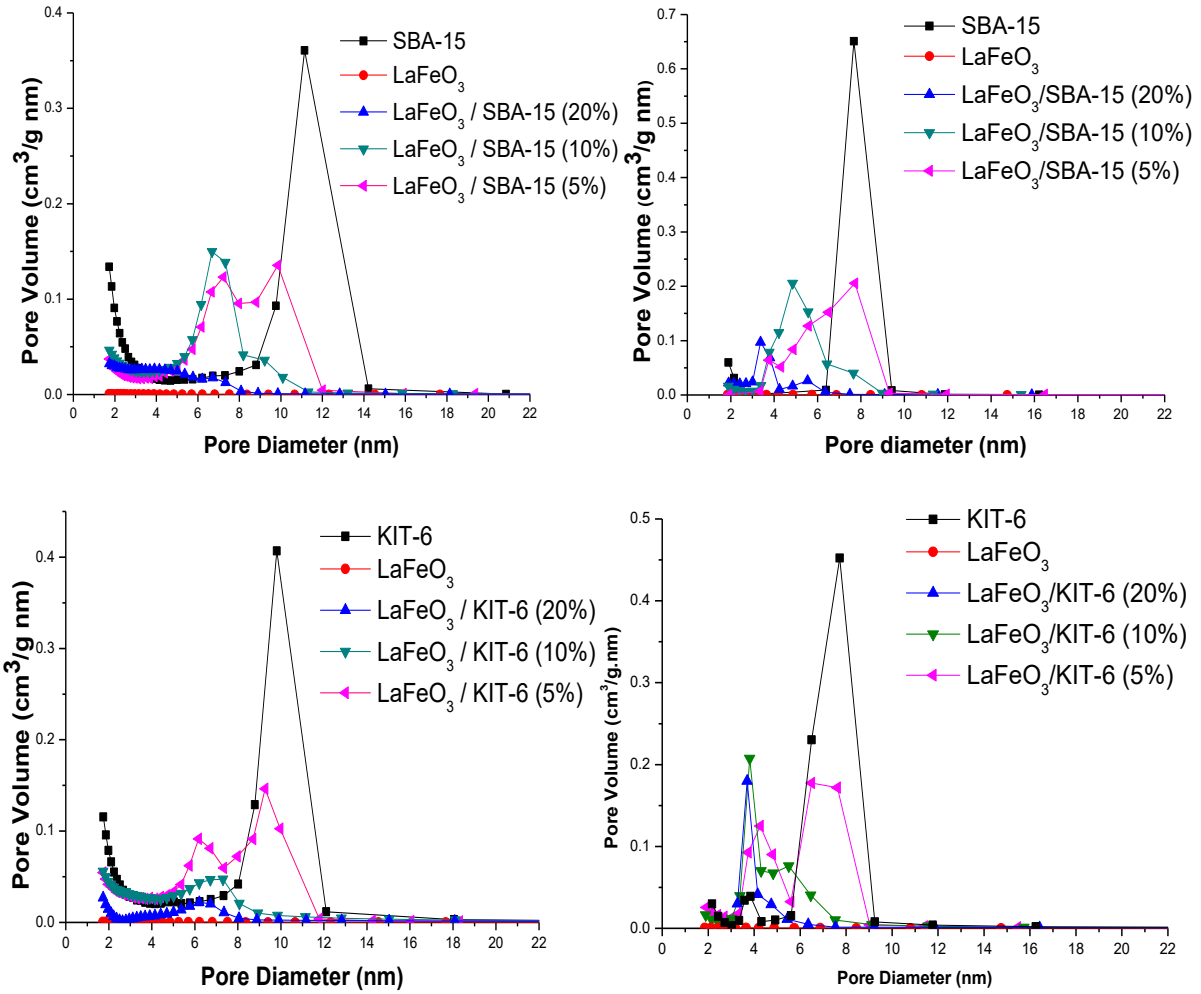


**Figure 28.** Pore size distribution of $LaFeO_3$/SBA-15 (top) and $LaFeO_3$/KIT-6 (bottom) catalysts: adsorption (left) and desorption (right)

The same effect seen in $TiO_2$ was observed for $LaFeO_3$, $BiFeO_3$, $AlFeO_3$ and $YFeO_3$ with both supports (Fig. 29-31 and Appendices) with isotherm changes following the same trends. In some cases with KIT-6, the samples suffered from cavitation, with pronounced artificial peaks around 4 nm in desorption PSDs.

These results are encouraging since it shows the procedure to deposit ferrites on SBA-15 and KIT-6 for all the ferrite samples was successful. While the behavior of $TiO_2$ into SBA-15 is quite different because the results from PSD suggests that the precursors are not completely inside the pores and it can be detected that some precursors can be outside the surface. In KIT-6, the presence of a peak around 3 nm in PSD shows that the incorporation of $TiO_2$ is in the intrawall pores concluding that the most of precursors are in the framework. Although, both

materials showed that there was not a total deposition of precursors in comparison with the ferrite samples as the results indicated in the PSDs.

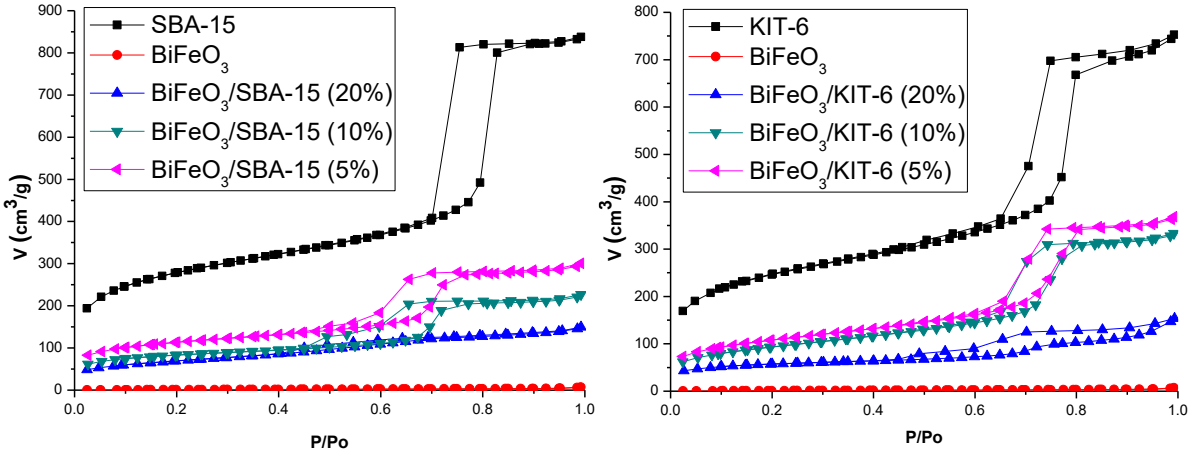


**Figure 29.** Nitrogen adsorption desorption isotherm for $BiFeO_3$ series catalysts: SBA-15 (left) and KIT-6 (right)

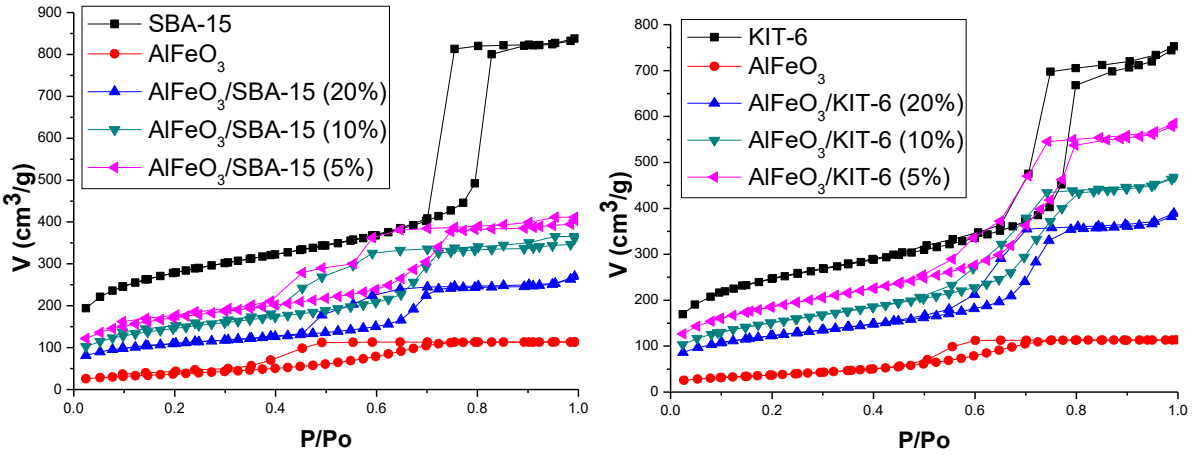


**Figure 30.** Nitrogen adsorption desorption isotherm $AlFeO_3$ catalysts: SBA-15 (left) and KIT-6 (right)

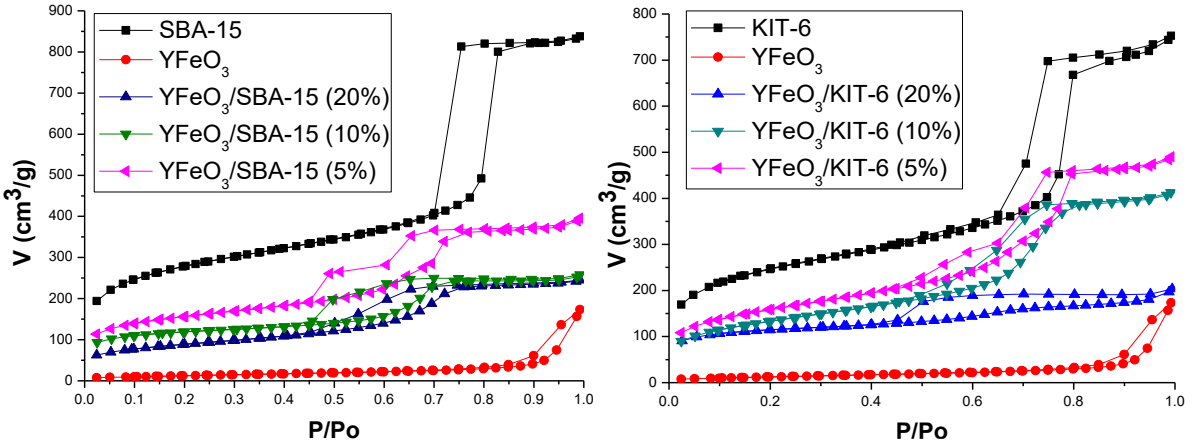


**Figure 31.** Nitrogen adsorption desorption isotherm for $YFeO_3$ series catalysts: SBA-15 (left) and KIT-6 (right)

### 4.2.2. X-Ray Diffraction (XRD)

Small-angle XRD patterns for the precursors ($TiO_2$, $LaFeO_3$, $BiFeO_3$, $AlFeO_3$, and $YFeO_3$) with SBA-15 and KIT-6 showed that the porous structure of the supports was not destroyed after the formation of the precursors. They conserved the characteristic peaks of the mesoporous silica lead to a decrease in peak intensity.[134] But the most notable changes are illustrated in the wide-angle XRD patterns of the samples. Because the wide-angle XRD gives information about the structure of the sample including the crystal phase, particle size, and peak position.

XRD patterns of $TiO_2$/SBA-15 are shown in Fig 32. The patterns evidenced the existence of titania in anatase structure corresponding to JCPDS No. 21-127. The anatase structure has characteristic peaks at 38°, 47°, 55°, 63° and an intense peak at 27.5°. The latter is ascribed to (101) plane and increase with the content of Ti species incorporated. There is an extra small peak around 23.5° corresponding to the rutile phase due to the high temperature of calcination (700 °C) indicating that there is a mixture of anatase and rutile phases. This is in agreement with the literature that thermal treatment influences the size and phase structure of the anatase phase.[135] When $TiO_2$/SBA-15 and $TiO_2$/KIT-6 are calcined at 700°C appear a pattern of amorphous and anatase respectively about $2\theta=25°$ increasing with relation to the Ti amount.[136]

The crystallite sizes were determined from the Scherrer's equation (equation 1) using the broadening of the (101) anatase peak reflection. The fact that one can observe XRD peaks of anatase with a crystallite size of 8.3 nm, 5.2 nm and, 8.9 nm for 5, 10, and 20% $TiO_2$ in SBA-15 and 7.4 nm, 9.1 nm and 10.6 nm for 5, 10, and 20% $TiO_2$ in KIT-6. The intensity of the (101) $TiO_2$ peaks decreases while the FWHM of (101) peaks increases in relation to the amount of Ti. The absence of titania features for low loading (5%) on SBA-15 and KIT-6 indicates the presence of highly dispersed titania into the structure.[137]

The use of KIT-6 and SBA-15 mesoporous support material appears to control the titania crystal size restricting the growing of the $TiO_2$ clusters inside the mesoporous channels at 5% loading. However, specific surface decreased gradually with the increase of titanium loading, but there is no specific trend on the average pore diameters. Therefore, it is accomplished that

the mesostructured is maintained upon $TiO_2$ addition into the pore of SBA-15 and KIT-6 silica materials.

These results are in agreement with what it found in PSD and adsorption-desorption isotherms that. $TiO_2$/SBA-15 and $TiO_2$/KIT-6 at 5% are possible to control the $TiO_2$ crystal size by constraining the growth of the titanium dioxide clusters inside the mesoporous channels. In contrast, the use of an amorphous support with 10% and 20% Ti load does not induce this effect, leading to bigger $TiO_2$ crystals as the titanium loading increases.[138] This indicates that titania is well dispersed inside mesoporous materials and causes partial blockage of its pore. The absence of reflection of crystalline $TiO_2$ at low titanium loading is due to the higher dispersion of titanium within the silica matrix, which can prevent the formation of $TiO_2$ domains sufficiently large to be detected by XRD.

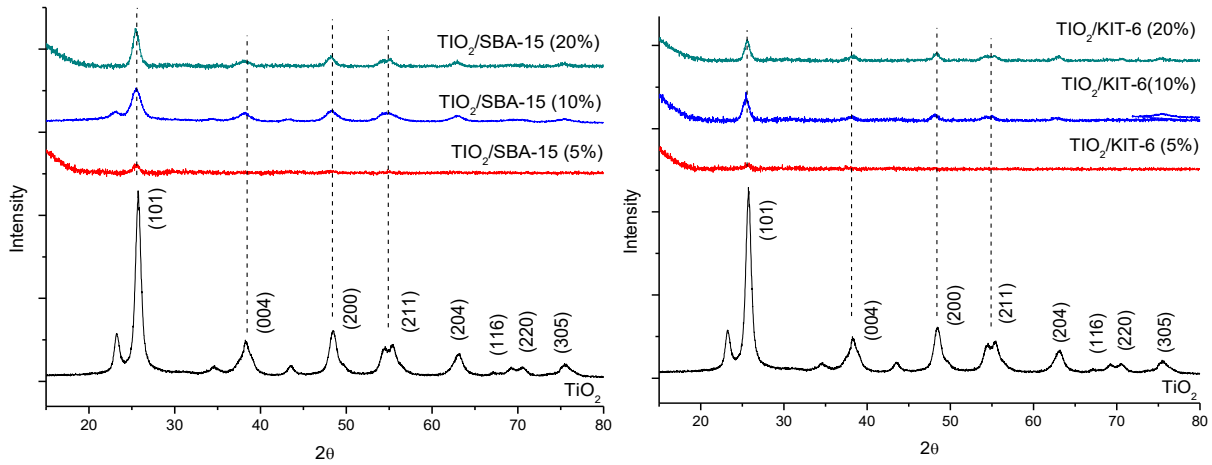


**Figure 32**. XRD patterns of $TiO_2$ catalysts with SBA-15 (left) and KIT-6 (right)

Fig. 33 displays the wide-angle XRD patterns of $LaFeO_3$/SBA-15 and $LaFeO_3$/KIT-6 series. The pattern shows a broad diffraction around 2θ=29° attributed to amorphous silica. No diffraction is observed for 5% $LaFeO_3$ loading. When the number of mixed oxides increases, there are peaks that appear at 2θ= 23.2, 32.5, 40.05, 58.3 and 67.9°. These peaks suggest the formation of $LaFeO_3$ crystallites.

They appear for 10% loading in SBA-15 and 20% loading in KIT-6. Below those percentages, $LaFeO_3$ seems well dispersed in the silica pore surface area. At 20% $LaFeO_3$/SBA-15, a new peak appears at 29.8° indicating the appearance of $La_2O_3$ phase.[139] These results demonstrate

that $LaFeO_3$ can disperse well, especially in the KIT-6 pore network, confirming the results from $N_2$ adsorption-desorption.

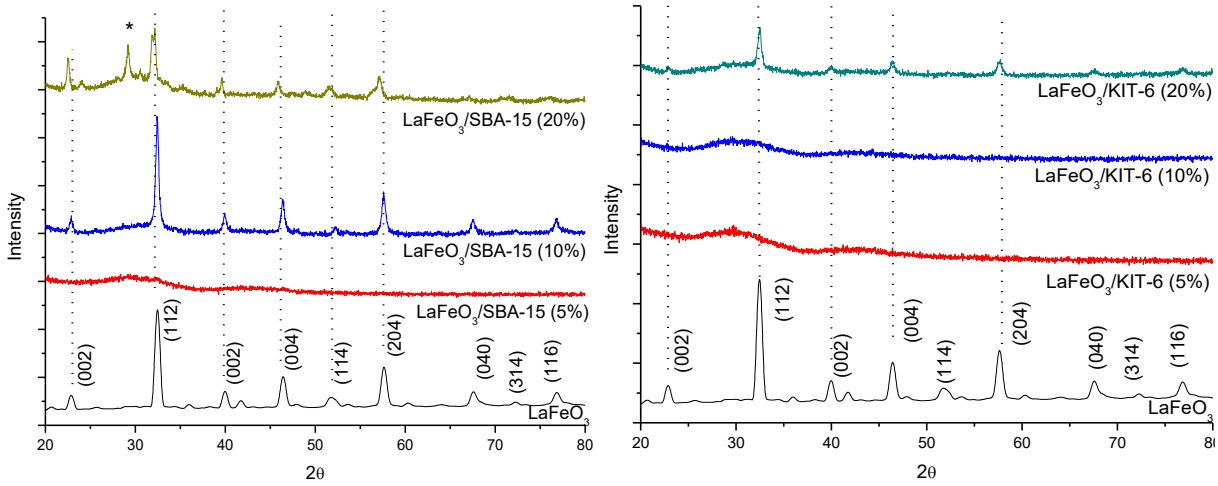


**Figure 33.** XRD patterns of $LaFeO_3$ catalysts with SBA-15 (left) and KIT-6 (right)

5-20% $BiFeO_3$/SBA-15 and $BiFeO_3$/KIT-6 series are presented in Fig 34. At 5% and 10%, the patterns have an amorphous nature determined by the silica (SBA-15 and KIT-6) that means that the material was well dispersed in the structure of the support. In the case of the $BiFeO_3$/SBA-15 and $BiFeO_3$/KIT-6 at 20%, both materials present characteristic peaks of $BiFeO_3$ at 2θ= 32.5°, 40.01°, 47.5°, 58.3° and 67.9° with high intensity. These results agree with those found in $N_2$ physisorption, in which isotherms showed a considerate decrease of pore size and volume.

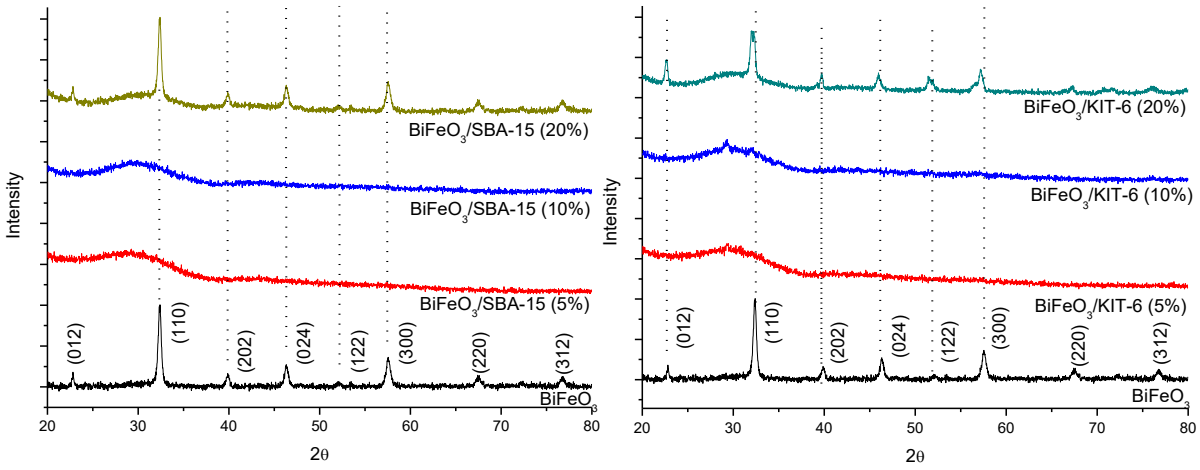


**Figure 34.** XRD patterns of $BiFeO_3$ catalysts with SBA-15 and KIT-6

5-20% $AlFeO_3$/SBA-15 (Fig. 35) series showed that samples are all amorphous, with only broad diffraction attributed to the silica. Even the unsupported pure $AlFeO_3$ did not show sharp peaks indicating that the $AlFeO_3$ powder is low crystallinity without other detectable phases, unlike $LaFeO_3$ and $BiFeO_3$ according to literature.[140]

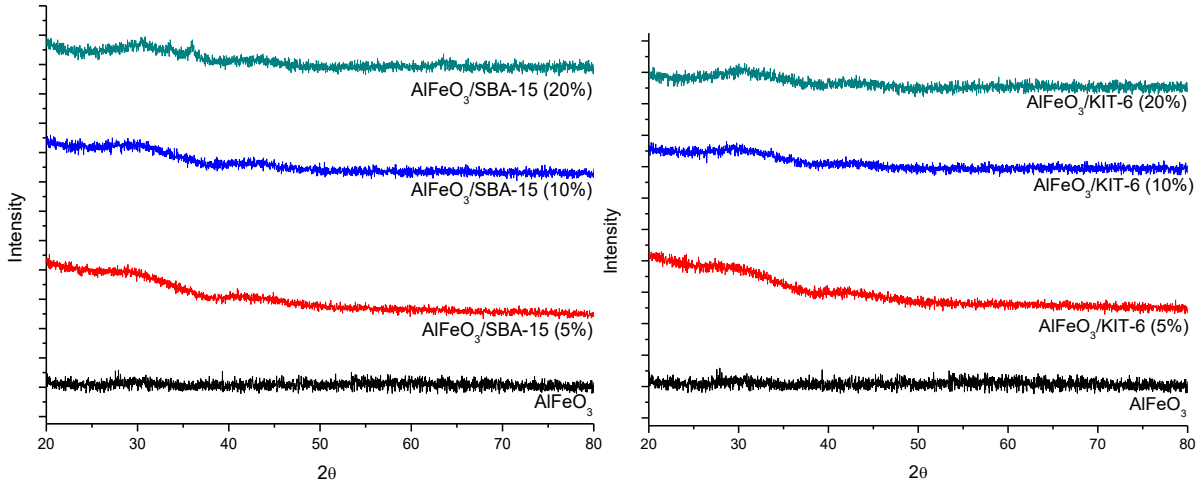


**Figure 35.** XRD patterns of $AlFeO_3$ with SBA-15 and KIT-6.

All samples $YFeO_3$/SBA-15 series and $YFeO_3$/KIT-6 series (Fig. 36) presented no diffraction peaks of perovskite, just a broad diffraction attributed to amorphous silica. These results seem to indicate that this precursor was highly dispersed in the structure, due to the absence of well-shaped peaks in both mesoporous supports.[141]

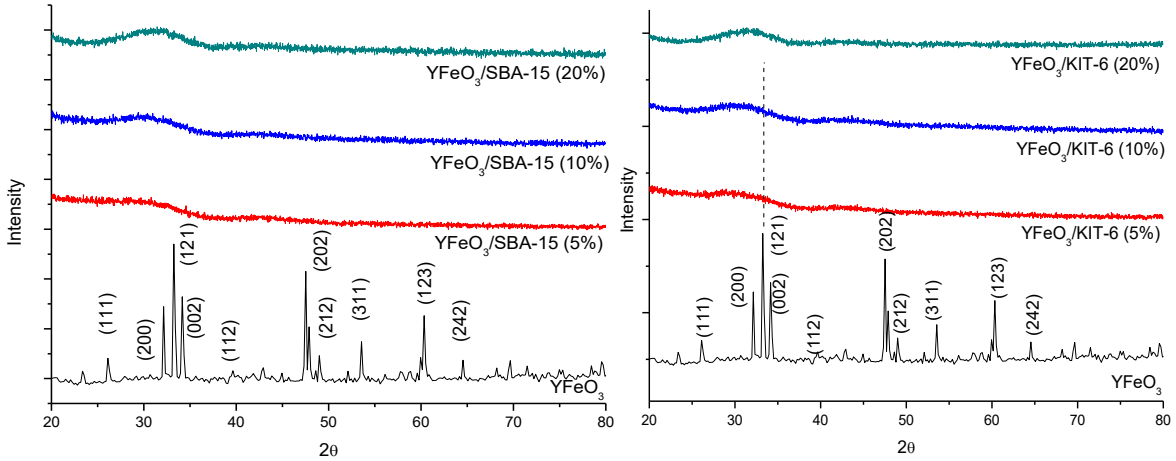


**Figure 36.** XRD patterns of $YFeO_3$ with SBA-15 and KIT-6

### 4.2.3. UV-visible spectroscopy (UV-vis DRS)

In this section, the study of the behavior of the bandgap of each semiconductor incorporated in the mesoporous silica was analyzed through UV-visible absorption. The purpose of the analysis is to verify the quantum size effect which leads to an increase in the bandgap (resulting in the blue shift).[142] When the bandgap increases, the conduction band edge position, and the valence band edge position shift upward and downward respectively, so the $E_{CB}$ will reach the suitable reduction potential from $CO_2$ to $CH_3OH$.

The visible light response and energy bandgap of the catalysts were investigated by UV-vis spectroscopy with a diffuse reflectance sphere. The Kubelka-Munk function was used to analyze the bandgap of each sample through the Tauc Plot and the conversion of eV from nm. Fig 37 shows the adsorption edges and band gap where the unsupported $TiO_2$ exhibited a bandgap approximately 3.34 eV resulting similar of the theoretical value of 3.20 eV as reported for anatase in the literature.[143]

The incorporation of $TiO_2$ inside the mesoporous materials gave a behavior effect where at 5% both SBA-15 and KIT-6 increase the bandgap instead of decreasing, (3.43 and 3.42 eV, respectively). These results may be not explained in terms of quantum size effects where the particle size decreases as the bandgap increases. We can attribute the shift of the band edge positions of $TiO_2/SiO_2$, as well as the increase in bandgap energy to electronic support interaction mediated though surface Si-O-Ti bonds and not to a quantum size effect.[144,145]

The quantum size effect did not show any tendency at 10 to 20% Ti amount where the band gap showed no significant change in the bandgap energy of 3.34 eV neither with SBA-15 nor KIT-6 when they are used as supports. This observation ensures that the lower crystallite size of $SiO_2$ as compared to $TiO_2$ has a negligible impact on the bandgap measurements and it is not the cause for the bandgap widening found in the supporting materials. This finding emphasizes the important role of the interface between $TiO_2$ and $SiO_2$.[146]

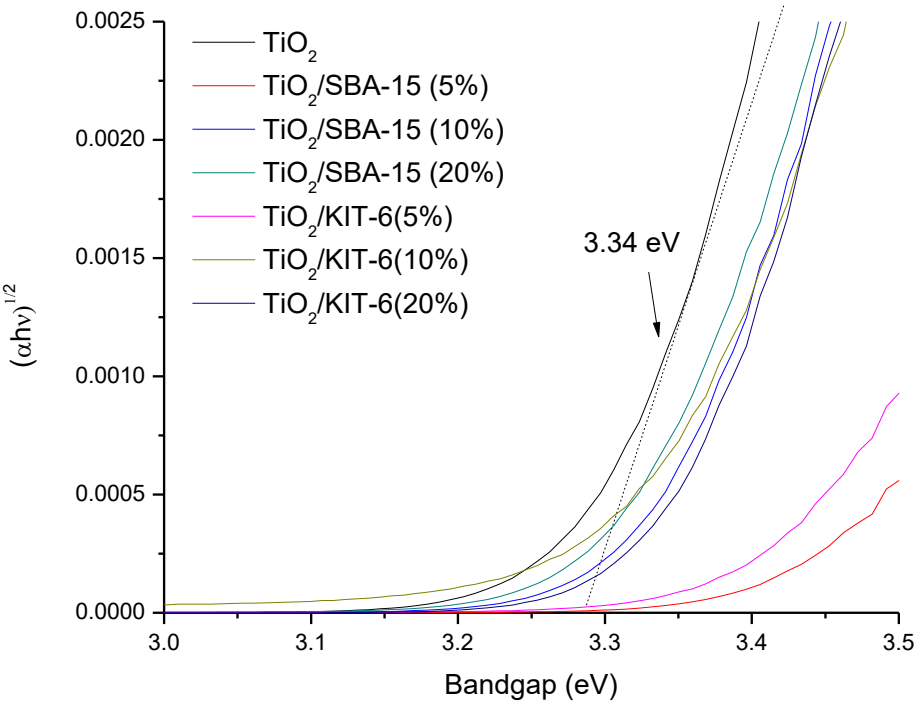


**Figure 37**. Uv-Vis spectrum of powder $TiO_2$ samples

The effect seen in the incorporation of $TiO_2$ is different than the perovskites when the $LaFeO_3$ is incorporated into the mesoporous support. Therefore, a load of species from 5% to 20% will lead to a significant change in the bandgap energy confirming a different effect than $TiO_2$ supported catalysts as it can be seen in Figure 38.[147]

The behavior can be explained in $LaFeO_3$ where we can see a change in the bandgap energy of the $LaFeO_3$ supported catalysts in SBA-15 at 5% (2.95 eV), 10% (2.53 eV), and 20% (2.31%). It can be observed a trend when the increase in the loading of $LaFeO_3$ into the SBA-15 support provokes an increase in the particle size as we can see in XRD results, and therefore the bandgap energy reduces. This results can confirm that the quantum size effect not only modifies the bandgap energy but only the VB and CB band edge position shift upward and downward respectively.

$BiFeO_3$, $YFeO_3$, and $AlFeO_3$ showed the same tendency as $LaFeO_3$, while the amount of a load of species in the material increases the band gap reduced its size explained by the quantum size effect. The Uv-visible spectrum of the semiconductor into silica support is illustrated in Appendix 7.2

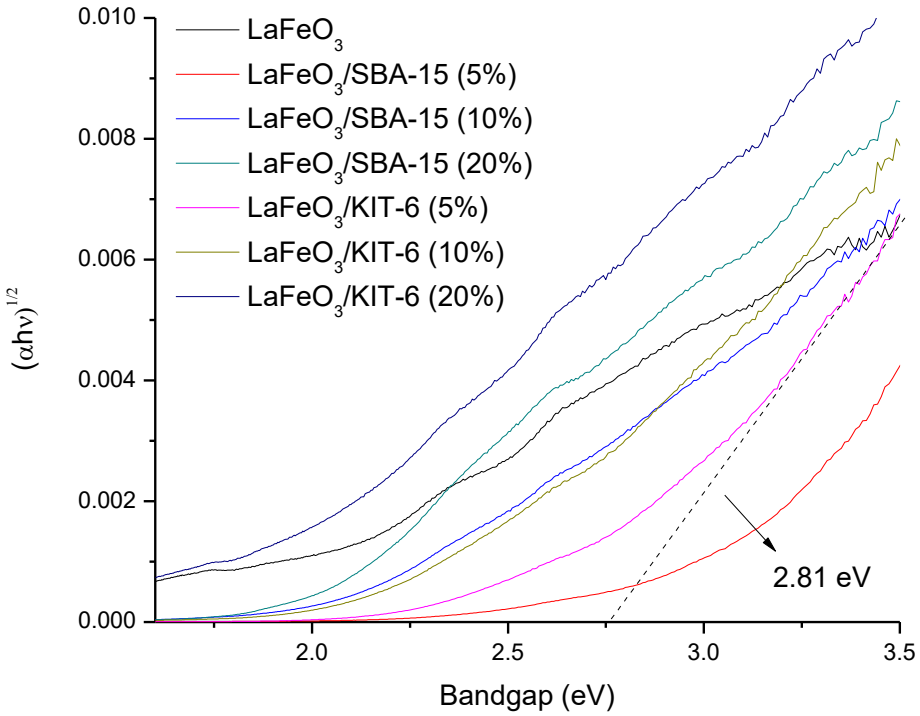


**Figure 38**. Uv-Vis spectrum of powder $LaFeO_3$ samples

These results suggest that the addition of SBA-15 and KIT-6 can effectively suppress the growth of particles and as a consequence of this the particles have a small size limited by the channels of the support.[148] Although in general these results should be taken with caution since it is difficult to avoid and quantify scattering effects during the data collection in these measurements. The same trend is shown in both supports SBA-15 and KIT-6, where the bandgap decreases when the particle size increases. As we can see in $TiO_2$ and perovskites, the election of different silica support did not show any significant change in the bandgap, and band edges position.

Table 4 shows the values for the valence band and the conduction band, calculated with the equations given (2) and (3) and the values of electronegativity (See Experimental). They were estimated to obtain an idea of the probable products to achieve considering the redox potentials of $CO_2$ and water conversions.

Table 4. Bandgap of photocatalysts

| | Sample | Bandgap structure (pH=7 vs NHE) | | |
|---|---|---|---|---|
| | | **Eg (eV)** | **CB** | **VB** |
| **1** | $TiO_2$ | 3.34 | -0.48 | 2.86 |
| **2** | $TiO_2$/SBA-15 (5%) | 3.43 | -0.53 | 2.91 |
| **3** | $TiO_2$/SBA-15 (10%) | 3.35 | -0.49 | 2.87 |
| **4** | $TiO_2$/SBA-15 (20%) | 3.34 | -0.48 | 2.86 |
| **5** | $TiO_2$/KIT-6 (5%) | 3.42 | -0.52 | 2.90 |
| **6** | $TiO_2$/KIT-6 (10%) | 3.34 | -0.48 | 2.86 |
| **7** | $TiO_2$/KIT-6 (20%) | 3.35 | -0.49 | 2.87 |
| **8** | $LaFeO_3$ | 2.12 | -0.02 | 2.10 |
| **9** | $LaFeO_3$/SBA-15 (5%) | 2.95 | -0.44 | 2.52 |
| **10** | $LaFeO_3$/SBA-15 (10%) | 2.53 | -0.23 | 2.31 |
| **11** | $LaFeO_3$/SBA-15 (20%) | 2.31 | -0.12 | 2.20 |
| **12** | $LaFeO_3$/KIT-6 (5%) | 2.81 | -0.37 | 2.45 |
| **13** | $LaFeO_3$/KIT-6 (10%) | 2.51 | -0.22 | 2.30 |
| **14** | $LaFeO_3$/KIT-6 (20%) | 2.20 | -0.06 | 2.14 |
| **15** | $BiFeO_3$ | 2.10 | 0.34 | 2.44 |
| **16** | $BiFeO_3$/SBA-15 (5%) | 2.54 | 0.12 | 2.66 |
| **17** | $BiFeO_3$/SBA-15 (10%) | 2.50 | 0.14 | 2.64 |
| **18** | $BiFeO_3$/SBA-15 (20%) | 2.46 | 0.16 | 2.62 |
| **19** | $BiFeO_3$/KIT-6 (5%) | 2.44 | 0.17 | 2.61 |
| **20** | $BiFeO_3$/KIT-6 (10%) | 2.28 | 0.25 | 2.53 |
| **21** | $BiFeO_3$/KIT-6 (20%) | 2.16 | 0.31 | 2.47 |
| **22** | $AlFeO_3$ | 1.71 | 0.26 | 1.97 |
| **23** | $AlFeO_3$/SBA-15 (5%) | 2.81 | -0.30 | 2.52 |
| **24** | $AlFeO_3$/SBA-15 (10%) | 2.69 | -0.24 | 2.46 |
| **25** | $AlFeO_3$/SBA-15 (20%) | 2.48 | -0.13 | 2.35 |
| **26** | $AlFeO_3$/KIT-6 (5%) | 2.62 | -0.20 | 2.42 |
| **27** | $AlFeO_3$/KIT-6 (10%) | 2.56 | -0.17 | 2.39 |
| **28** | $AlFeO_3$/KIT-6 (20%) | 2.22 | 0.00 | 2.22 |
| **29** | $YFeO_3$ | 2.25 | -0.01 | 2.25 |
| **30** | $YFeO_3$/SBA-15 (5%) | 2.99 | -0.38 | 2.62 |
| **31** | $YFeO_3$/SBA-15 (10%) | 2.94 | -0.35 | 2.59 |
| **32** | $YFeO_3$/SBA-15 (20%) | 2.57 | -0.17 | 2.41 |
| **33** | $YFeO_3$/KIT-6 (5%) | 2.73 | -0.25 | 2.49 |
| **34** | $YFeO_3$/KIT-6 (10%) | 2.70 | -0.23 | 2.47 |
| **35** | $YFeO_3$/KIT-6 (20%) | 2.64 | -0.20 | 2.44 |

Figure 39 shows the bandgap (Eg) and the position of the edges according to the information given in Table 4. For four samples the incorporation of the species at low levels 5% increased the bandgap substantially to the point that the CB is positioned above the $CO_2$ to methanol reduction potential. However, this will also decrease the amount of solar light they can absorb.

$BiFeO_3$ perovskites failed to get the appropriate band edges in both SBA-15 and KIT-6 at different amounts. This is due to the positive redox potential in $E_{CB}$ whose values are below the $CO_2$ reduction potential to thermodynamically conversion to $CH_3OH$ ($E_{CB}$ = 0.12) as we can see in Table 4. This can be explained because the reduction of $CO_2$ to hydrocarbons requires that the bottom energy level of $E_{CB}$ needs to be more negative with respect to reduction potential for $CO_2$. The yields of methanol are well correlated with the CB edge position of the semiconductors, indicating the necessary requirement of a negative CB edge relative to the $CO_2/CH_3OH$ reduction potential. Moreover, we can observe that these materials are not suitable for water splitting ($E_{CB}$= 0.00) as well.[149]

However, $LaFeO_3$ at 10% (SBA-15 and KIT-6), and $YFeO_3$ at 5% and 10% (SBA-15) have the suitable CB and VB to provide sufficient negative and positive redox potentials for water oxidation and $CO_2$ reduction. Their bandgaps are below 3 eV, appropriate to absorb the visible light in comparison with $TiO_2$. Although $TiO_2$ materials in both silica support reached the ECB position for the $CO_2/CH_3OH$ conversion, their large bandgap energy (>3.2 eV) will not coincide with the visible spectrum. Their large bandgap will absorb in the UV region that corresponds to only 4% to the incident solar energy, which limits the spectrum of photons that can create electron-hole pairs to participate in oxidation or reduction reactions.[150]

With this information, we can suggest that $LaFeO_3$/SBA-15 (5%), $LaFeO_3$/KIT-6 (5%) and $YFeO_3$/SBA-15 (5%), $YFeO_3$/SBA-15 (10%) have the appropriate band edges and bandgap to absorb in the visible light range.

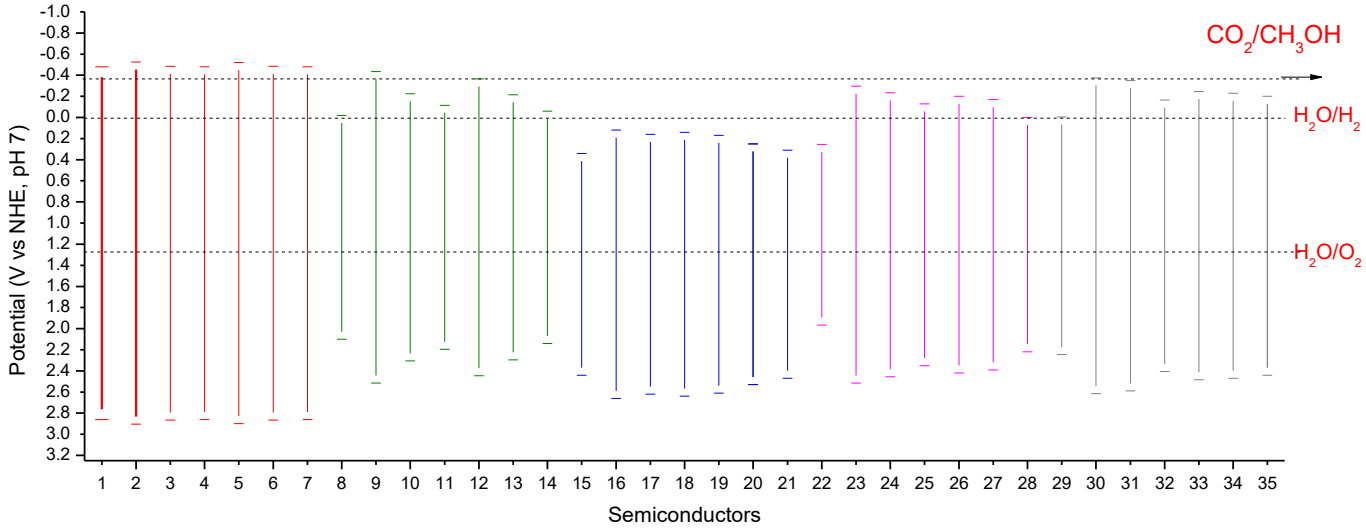


**Figure 39.** Conduction band (CB) and valence band (VB) of semiconductors. X-axis number refer to Table 4.

## 5. CONCLUSIONS

The main conclusions of this MPhil are:

The preparation of SBA-15 and KIT-6 were successfully synthesized using the hydrothermal method and calcination at 550 °C. They showed high specific surface area (933 and 833 $m^2/g$ respectively), pore size about 7 nm and the low angle XRD patterns presented the characteristic peaks confirming that the materials are of suitable structure and ordered mesoporosity. These characteristics make the supports as good candidates to be a host of metal oxides not only to accommodate $CO_2$ but also the perovskites.

Synthesis of the perovskites $LaFeO_3$, $BiFeO_3$, and $YFeO_3$ have been successfully produced by the sol-gel method and confirmed by XRD. Additionally, the preparation of the perovskites in the presence of the mesoporous material was carried out following a sol-gel method at 75°C and calcination at 550°C. The formation of a ferrite-silica composite was confirmed by the appearance of characteristic peaks in XRD for high loadings such as 20%, with the exception of the $AlFeO_3$ sample.

Furthermore, $TiO_2$ loading on SBA-15 and KIT-6 was also attempted and the presence of $TiO_2$ anatase and rutile confirmed by XRD. At low loadings, the $TiO_2$ and ferrite perovskites were well dispersed into $SiO_2$ supports. The increment of loading of the precursors (10% and 20%)

cause the rise of mean peaks of each ferrite perovskites. This effect causes the partial destruction of the structure of the support inducing the increase of particle size that provokes the decreasing of the bandgap energy, and therefore the contraction of $E_{CB}$ for $CO_2/CH_3OH$ conversion.

In $N_2$ adsorption-desorption technique, the catalysts with perovskites showed the loss of specific surface area around 73% due to the increase in the percentage of mixed ferrite up to 20%. The PSDs confirmed the dispersion of ferrite species into the SBA-15 and KIT-6, with narrower pore bodies and necks. There was a clear correlation between ferrite perovskite loading and shrinkage of pore sizes. However, crystallites outside the pore network were present, as confirmed by XRD. KIT-6 loaded with ferrites showed nitrogen cavitation effects, which could lead to poorer diffusion of $CO_2$ and the resulting products.

From UV-vis spectroscopy, it is concluded that $LaFeO_3$/SBA-15 and $LaFeO_3$/SBA-15 at 5% and $YFeO_3$/SBA-15 at 5% and 10% have the suitable CB and VB edges to reduce $CO_2$ with water to methanol and the narrow bandgap to absorb the visible light. $BiFeO_3$/SBA-15 and $BiFeO_3$/KIT-6 showed, however, narrower bandgap convenient to absorb in the visible range but a CB not suitable for $CO_2/CH_3OH$.

Concluding, 5% loading was found to be the best loading to achieve a good dispersion of photocatalysts inside SBA-15 or KIT-6. Both supports behave similarly, although the KIT-6 pore network was easier to get blocked due to the presence of narrower necks. Future experiments should be directed towards studying loading around 5% and in testing these composites in the photocatalytic $CO_2$ reduction. To this end, a photocatalytic reactor with a quartz window for the simulated sunlight irradiation and control over humidity and mass flow of $CO_2$ will be needed.

# 6. REFERENCES


1. S.R. Lingampalli, M.M. Ayyub, C.N.R. Rao, Recent Progress in the Photocatalytic Reduction of Carbon Dioxide, ACS Omega. 2 (2017) 2740–2748.
2. Introduction to Industrial carbon capture and storage, Global CCS Institute. (2016).
3. K. Kalyanasundaram, M. Graetzel, Artificial photosynthesis: biomimetic approaches to solar energy conversion and storage, Current Opinion in Biotechnology. 21 (6) 298–310. doi:10.1016/j.copbio.2010.03.021.
4. R. Blankenship, Molecular Mechanisms of Photosynthesis, in: Wiley-Blackwell (Ed.), Second Edition, 2014: p. 312.
5. D.C. Grills, E. Fujita, New Directions for the Photocatalytic Reduction of CO2: Supramolecular, scCO2 or Biphasic Ionic Liquid−scCO2 Systems, The Journal of Physical Chemistry Letters. 1 (2010) 2709–2718. doi:10.1021/jz1010237.
6. S. Dutch, Carbon Dioxide, (1997). https://www.uwgb.edu/dutchs/Petrology/CO2.HTM.
7. S. Xie, Q. Zhang, G. Liu, Y. Wang, Photocatalytic and photoelectrocatalytic reduction of CO2 using heterogeneous catalysts with controlled nanostructures, Chemical Communications. 52 (2016) 35–59. doi:10.1039/C5CC07613G.
8. P. Usubharatana, D. McMartin, A. Veawab, P. Tontiwachwuthikul, Photocatalytic process for CO2 emission reduction from industrial flue gas streams, Industrial & Engineering Chemistry Research. 45 (2006) 2558–2568.
9. I.E.A.O. of E. Technology, D., G. of Eight, Energy technology perspectives, International Energy Agency, 2008.
10. P. Luckow, M.A. Wise, J.J. Dooley, S.H. Kim, Large-scale utilization of biomass energy and carbon dioxide capture and storage in the transport and electricity sectors under stringent CO2 concentration limit scenarios, International Journal of Greenhouse Gas Control. 4 (2010) 865–877. doi:10.1016/j.ijggc.2010.06.002.
11. Policymeasures.com, Carbon Capture and Storage, (2017). http://www.policymeasures.com/measures/detail/carbon-capture-and-storage.
12. A.J. Morris, G.J. Meyer, E. Fujita, Molecular Approaches to the Photocatalytic Reduction of Carbon Dioxide for Solar Fuels, Accounts of Chemical Research. 42 (2009) 1983–1994. doi:10.1021/ar9001679.
13. Y.-X. Pan, Y. You, S. Xin, Y. Li, G. Fu, Z. Cui, Y.-L. Men, F.-F. Cao, S.-H. Yu, J.B. Goodenough, Photocatalytic CO2 Reduction by Carbon-Coated Indium-Oxide Nanobelts, Journal of the American Chemical Society. 139 (2017) 4123–4129. doi:10.1021/jacs.7b00266.
14. J. Wen, J. Xie, X. Chen, X. Li, A review on g-C3N4-based photocatalysts, Applied Surface Science. 391, Part B (Enero 1) 72–123. doi:10.1016/j.apsusc.2016.07.030.

15. M.R. Hasan, S.B.A. Hamid, W.J. Basirun, Charge transfer behavior of graphene-titania photoanode in CO2 photoelectrocatalysis process, Applied Surface Science. 339 (2015) 22–27. doi:10.1016/j.apsusc.2015.02.162.

16. J. Zhao, X. Wang, Z. Xu, J.S.C. Loo, Hybrid catalysts for photoelectrochemical reduction of carbon dioxide: a prospective review on semiconductor/metal complex co-catalyst systems, Journal of Materials Chemistry A. 2 (2014) 15228–15233. doi:10.1039/C4TA02250E.

17. A. Mills, S. Le Hunte, An overview of semiconductor photocatalysis, Journal of Photochemistry and Photobiology A: Chemistry. 108 (1997) 1–35.

18. Y. Izumi, Recent advances in the photocatalytic conversion of carbon dioxide to fuels with water and/or hydrogen using solar energy and beyond, Coordination Chemistry Reviews. 257 (2013) 171–186.

19. R. Shi, G.I. Waterhouse, T. Zhang, Recent progress in photocatalytic CO2 reduction over perovskite oxides, Solar RRL. (2017).

20. B. Yacobi, Band Theory of Solids, Semiconductor Materials: An Introduction to Basic Principles. (2003) 33–58.

21. J.Y. Do, Y. Im, B.S. Kwak, J.-Y. Kim, M. Kang, Dramatic CO2 photoreduction with H2O vapors for CH4 production using the TiO2 (bottom)/Fe–TiO2 (top) double-layered films, Chemical Engineering Journal. 275 (Enero 9) 288–297. doi:10.1016/j.cej.2015.03.066.

22. Fundamentals of Electrical Engineering, 2nd ed., Oxford UP, New York, 1996.

23. C.J. Rhodes, Zeolites: physical aspects and environmental applications, Annual Reports Section" C"(Physical Chemistry). 103 (2007) 287–325.

24. N. Gargiulo, F. Pepe, D. Caputo, CO2 adsorption by functionalized nanoporous materials: a review, Journal of Nanoscience and Nanotechnology. 14 (2014) 1811–1822.

25. K. Ikeue, H. Yamashita, M. Anpo, T. Takewaki, Photocatalytic reduction of CO2 with H2O on Ti− β zeolite photocatalysts: Effect of the hydrophobic and hydrophilic properties, The Journal of Physical Chemistry B. 105 (2001) 8350–8355.

26. M. Anpo, Photocatalytic reduction of CO2 with H2O on highly dispersed Ti-oxide catalysts as a model of artificial photosynthesis, Journal of CO2 Utilization. 1 (2013) 8–17.

27. Y. Li, W.-N. Wang, Z. Zhan, M.-H. Woo, C.-Y. Wu, P. Biswas, Photocatalytic reduction of CO2 with H2O on mesoporous silica supported Cu/TiO2 catalysts, Applied Catalysis B: Environmental. 100 (2010) 386–392. doi:10.1016/j.apcatb.2010.08.015.

28. G. Liu, N. Hoivik, K. Wang, H. Jakobsen, Engineering TiO2 nanomaterials for CO2 conversion/solar fuels, Solar Energy Materials and Solar Cells. 105 (2012) 53–68. doi:10.1016/j.solmat.2012.05.037.

29. N. Suzuki, S. Kiba, Y. Yamauchi, Fabrication of mesoporous silica KIT-6/polymer composite and its low thermal expansion property, Materials Letters. 65 (2) 544–547. doi:10.1016/j.matlet.2010.10.027.

30. R. Atluri, Y. Sakamoto, A.E. Garcia-Bennett, Co-structure directing agent induced phase transformation of mesoporous materials, Langmuir. 25 (2009) 3189–3195.

31. R. Atluri, N. Hedin, A.E. Garcia-Bennett, Hydrothermal phase transformation of bicontinuous cubic mesoporous material AMS-6, Chemistry of Materials. 20 (2008) 3857–3866.

32. R. Atluri, Z. Bacsik, N. Hedin, A.E. Garcia-Bennett, Structural variations in mesoporous materials with cubic $Pm3^{-}n$ symmetry, Microporous and Mesoporous Materials. 133 (2010) 27–35.

33. A. Taguchi, F. Schüth, Ordered mesoporous materials in catalysis, Microporous and Mesoporous Materials. 77 (Marzo 1) 1–45. doi:10.1016/j.micromeso.2004.06.030.

34. M. Impéror-Clerc, P. Davidson, A. Davidson, Existence of a Microporous Corona around the Mesopores of Silica-Based SBA-15 Materials Templated by Triblock Copolymers, Journal of the American Chemical Society. 122 (2000) 11925–11933. doi:10.1021/ja002245h.

35. J. Yang, J. Zhang, L. Zhu, S. Chen, Y. Zhang, Y. Tang, Y. Zhu, Y. Li, Synthesis of nano titania particles embedded in mesoporous SBA-15: Characterization and photocatalytic activity, Journal of Hazardous Materials. 137 (9) 952–958. doi:10.1016/j.jhazmat.2006.03.017.

36. F. Jiao, A.H. Hill, A. Harrison, A. Berko, A.V. Chadwick, P.G. Bruce, Synthesis of Ordered Mesoporous NiO with Crystalline Walls and a Bimodal Pore Size Distribution, Journal of the American Chemical Society. 130 (2008) 5262–5266. doi:10.1021/ja710849r.

37. K. Soni, B.S. Rana, A.K. Sinha, A. Bhaumik, M. Nandi, M. Kumar, G.M. Dhar, 3-D ordered mesoporous KIT-6 support for effective hydrodesulfurization catalysts, Applied Catalysis B: Environmental. 90 (7) 55–63. doi:10.1016/j.apcatb.2009.02.010.

38. F. Subhan, S. Aslam, Z. Yan, M. Ikram, S. Rehman, Enhanced desulfurization characteristics of Cu-KIT-6 for thiophene, Microporous and Mesoporous Materials. 199 (11) 108–116. doi:10.1016/j.micromeso.2014.08.018.

39. C. Jo, K. Kim, R. Ryoo, Syntheses of high quality KIT-6 and SBA-15 mesoporous silicas using low-cost water glass, through rapid quenching of silicate structure in acidic solution, Microporous and Mesoporous Materials. 124 (2009) 45–51.

40. S. Ruthstein, J. Schmidt, E. Kesselman, Y. Talmon, D. Goldfarb, Resolving intermediate solution structures during the formation of mesoporous SBA-15, Journal of the American Chemical Society. 128 (2006) 3366–3374.

41. K. Flodström, V. Alfredsson, Influence of the block length of triblock copolymers on the formation of mesoporous silica, Microporous and Mesoporous Materials. 59 (2003) 167–176.

42. V.F. Vavsari, G.M. Ziarani, A. Badiei, The role of SBA-15 in drug delivery, RSC Advances. 5 (2015) 91686–91707.

43. I.P. Suzdalev, Nanotechnology. Physico-chemistry of nanoclusters, nanostructures and nanomaterials, 2005.

44. V. Alfredsson, H. Wennerström, The Dynamic Association Processes Leading from a Silica Precursor to a Mesoporous SBA-15 Material, Accounts of Chemical Research. 48 (2015) 1891–1900. doi:10.1021/acs.accounts.5b00165.

45. Y. Sakamoto, M. Kaneda, O. Terasaki, D.Y. Zhao, J.M. Kim, G. Stucky, H.J. Shin, R. Ryoo, Direct imaging of the pores and cages of three-dimensional mesoporous materials, Nature. 408 (2000) 449–453. doi:10.1038/35044040.

46. A.G. Denkova, E. Mendes, M.O. Coppens, Effects of Salts and Ethanol on the Population and Morphology of Triblock Copolymer Micelles in Solution, The Journal of Physical Chemistry B. 112 (2008) 793–801. doi:10.1021/jp075114c.

47. M.A. Ballem, E.M. Johansson, J.M. Córdoba, M. Odén, Synthesis of hollow silica spheres SBA-16 with large-pore diameter, Materials Letters. 65 (2011) 1066–1068. doi:10.1016/j.matlet.2011.01.035.

48. N. Reichhardt, T. Kjellman, M. Sakeye, F. Paulsen, J.-H. Smått, M. Lindén, V. Alfredsson, Removal of Intrawall pores in SBA-15 by selective modification, Chemistry of Materials. 23 (2011) 3400–3403.

49. O. Carp, C.L. Huisman, A. Reller, Photoinduced reactivity of titanium dioxide, Progress in Solid State Chemistry. 32 (//) 33–177. doi:10.1016/j.progsolidstchem.2004.08.001.

50. N. Greenwood, A. Earnshaw, Chemistry of the Elements, 1997.

51. V. Etacheri, C. Di Valentin, J. Schneider, D. Bahnemann, S.C. Pillai, Visible-light activation of TiO 2 photocatalysts: advances in theory and experiments, Journal of Photochemistry and Photobiology C: Photochemistry Reviews. 25 (2015) 1–29.

52. V. Subramanian, E.E. Wolf, P.V. Kamat, Catalysis with TiO2/Gold Nanocomposites. Effect of Metal Particle Size on the Fermi Level Equilibration, Journal of the American Chemical Society. 126 (2004) 4943–4950. doi:10.1021/ja0315199.

53. Y. Ku, K. Tseng, C. Ma, Photocatalytic decomposition of gaseous acetone using TiO2 and Pt/TiO2 catalysts, International Journal of Chemical Kinetics. 40 (2008) 209–216.

54. H. Park, Y. Park, W. Kim, W. Choi, Surface modification of TiO2 photocatalyst for environmental applications, Journal of Photochemistry and Photobiology C: Photochemistry Reviews. 15 (2013) 1–20. doi:10.1016/j.jphotochemrev.2012.10.001.

55. W. Mai, F. Wen, D. Xie, Y. Leng, Z. Mu, Structure and composition study of carbon-doped titanium oxide film combined with first principles, Journal of Advanced Ceramics. 3 (2014) 49–55. doi:10.1007/s40145-014-0092-2.

56. M.S. Vohra, K. Tanaka, Photocatalytic degradation of aqueous pollutants using silica-modified TiO2, Water Research. 37 (2003) 3992–3996.

57. X. Chang, T. Wang, J. Gong, CO2 photo-reduction: insights into CO2 activation and reaction on surfaces of photocatalysts, Energy & Environmental Science. 9 (2016) 2177–2196. doi:10.1039/C6EE00383D.

58. A. Trenczek-Zając, J. Banaś, K. Świerczek, K. Zazakowny, M. Radecka, Photosensitization of TiO2 P25 with CdS Nanoparticles for Photocatalytic Applications, Amm. 62 (2017) 841. doi:10.1515/amm-2017-0124.

59. M.M. Lee, J. Teuscher, T. Miyasaka, T.N. Murakami, H.J. Snaith, Efficient hybrid solar cells based on meso-superstructured organometal halide perovskites, Science. 338 (2012) 643–647.

60. J. Yang, H. Zhong, M. Li, L. Zhang, Y. Zhang, Markedly enhancing the visible-light photocatalytic activity of LaFeO3 by post-treatment in molten salt, Reaction Kinetics and Catalysis Letters. 97 (2009) 269–274. doi:10.1007/s11144-009-0025-1.

61. H. Zhu, P. Zhang, S. Dai, Recent Advances of Lanthanum-Based Perovskite Oxides for Catalysis, ACS Catalysis. 5 (2015) 6370–6385. doi:10.1021/acscatal.5b01667.

62. T. Ishihara, Structure and Properties of Perovskite Oxides, in: T. Ishihara (Ed.), Perovskite Oxide for Solid Oxide Fuel Cells, Springer US, Boston, MA, 2009: pp. 1–16. doi:10.1007/978-0-387-77708-5_1.

63. D.Q. Fei, T. Hudaya, A.A. Adesina, Visible-light activated titania perovskite photocatalysts: Characterization and initial activity studies, Catalysis Communications. 6 (2005) 253–258.

64. M.M. Shirolkar, C. Hao, X. Dong, T. Guo, L. Zhang, M. Li, H. Wang, Tunable multiferroic and bistable/complementary resistive switching properties of dilutely Li-doped BiFeO3 nanoparticles: an effect of aliovalent substitution, Nanoscale. 6 (2014) 4735–4744. doi:10.1039/C3NR05973A.

65. K.L. Hardee, A.J. Bard, Semiconductor electrodes X. Photoelectrochemical behavior of several polycrystalline metal oxide electrodes in aqueous solutions, Journal of the Electrochemical Society. 124 (1977) 215–224.

66. J.K. Leland, A.J. Bard, Photochemistry of colloidal semiconducting iron oxide polymorphs, Journal of Physical Chemistry. 91 (1987) 5076–5083.

67. Y. Lin, G. Yuan, S. Sheehan, S. Zhou, D. Wang, Hematite-based solar water splitting: challenges and opportunities, Energy & Environmental Science. 4 (2011) 4862–4869.

68. P. Kanhere, Z. Chen, A review on visible light active perovskite-based photocatalysts, Molecules. 19 (2014) 19995–20022.

69. I.R. Shein, K.I. Shein, V.L. Kozhevnikov, A.L. Ivanovskii, Band structure and the magnetic and elastic properties of SrFeO3 and LaFeO3 perovskites, Physics of the Solid State. 47 (2005) 2082–2088. doi:10.1134/1.2131149.

70. K. Peng, L. Fu, H. Yang, J. Ouyang, Perovskite LaFeO3/ montmorillonite nanocomposites: synthesis, interface characteristics and enhanced photocatalytic activity, Scientific Reports. 6 (2016) 19723. doi:10.1038/srep19723.

71. O. Madelung, U. Rössler, M. Schulz, eds., LaFeO3 crystal structure, physical properties, in: Ternary Compounds, Organic Semiconductors, Springer Berlin Heidelberg, Berlin, Heidelberg, 2000: pp. 1–4. doi:10.1007/10717201_1110.

72. P. Tang, Y. Tong, H. Chen, F. Cao, G. Pan, Microwave-assisted synthesis of nanoparticulate perovskite LaFeO3 as a high active visible-light photocatalyst, Current Applied Physics. 13 (3) 340–343. doi:10.1016/j.cap.2012.08.006.

73. B.S. Liu, X.N. Wei, Y.P. Zhan, R.Z. Chang, F. Subhan, C.T. Au, Preparation and desulfurization performance of LaMeOx/SBA-15 for hot coal gas, Applied Catalysis B: Environmental. 102 (2011) 27–36. doi:10.1016/j.apcatb.2010.11.020.

74. D.-C. Jia, J.-H. Xu, H. Ke, W. Wang, Y. Zhou, Structure and multiferroic properties of BiFeO3 powders, Journal of the European Ceramic Society. 29 (11) 3099–3103. doi:10.1016/j.jeurceramsoc.2009.04.023.

75. T. Gao, Z. Chen, Y. Zhu, F. Niu, Q. Huang, L. Qin, X. Sun, Y. Huang, Synthesis of BiFeO3 nanoparticles for the visible-light induced photocatalytic property, Materials Research Bulletin. 59 (11) 6–12. doi:10.1016/j.materresbull.2014.06.022.

76. P.S.V. Mocherla, C. Karthik, R. Ubic, M.S.R. Rao, C. Sudakar, Tunable bandgap in BiFeO3 nanoparticles: The role of microstrain and oxygen defects, Applied Physics Letter. 103 (2013) 022910.

77. F. Kubel, H. Schmid, Structure of a ferroelectric and ferroelastic monodomain crystal of the perovskite BiFeO3, Acta Crystallographica Section B: Structural Science. 46 (1990) 698–702.

78. H. Naganuma, Multifunctional Characteristics of B-site Substituted BiFeO3 Films, in: M. Lallart (Ed.), Ferroelectrics - Physical Effects, InTech, Rijeka, 2011: p. Ch. 16. doi:10.5772/17538.

79. R. Saha, A. Shireen, S.N. Shirodkar, M.S. Singh, U.V. Waghmare, A. Sundaresan, C.N.R. Rao, Phase Transitions of AlFeO3 and GaFeO3 from the Chiral Orthorhombic (Pna21) Structure to the Rhombohedral ($R\bar{3}c$) Structure, Inorganic Chemistry. 50 (2011) 9527–9532. doi:10.1021/ic201235h.

80. P. Tang, H. Chen, F. Cao, G. Pan, Magnetically recoverable and visible-light-driven nanocrystalline YFeO3 photocatalysts, Catalysis Science & Technology. 1 (2011) 1145–1148. doi:10.1039/C1CY00199J.

81. V.G. Nair, A. Das, V. Subramanian, P. Santhosh, Magnetic structure and magnetodielectric effect of YFe0. 5Cr0. 5O3, Journal of Applied Physics. 113 (2013) 213907.

82. M.I. Díez-García, V. Celorrio, L. Calvillo, D. Tiwari, R. Gómez, D.J. Fermín, YFeO3 Photocathodes for Hydrogen Evolution, Electrochimica Acta. (n.d.). doi:10.1016/j.electacta.2017.06.025.

83. J. Vernimmen, Synthesis of titanium-activated siliceous materials with a combined micro-and mesoproosity, Universiteit Antwerpen (Belgium), 2011.

84. X. Li, H. Liu, D. Luo, J. Li, Y. Huang, H. Li, Y. Fang, Y. Xu, L. Zhu, Adsorption of CO2 on heterostructure CdS(Bi2S3)/TiO2 nanotube photocatalysts and their photocatalytic activities in the reduction of CO2 to methanol under visible light irradiation, Chemical Engineering Journal. 180 (2012) 151–158.

85. M.A.A. Aziz, A.A. Jalil, S. Triwahyono, A. Ahmad, CO2 methanation over heterogeneous catalysts: recent progress and future prospects, Green Chemistry. 17 (2015) 2647–2663.

86. R. Srivastava, D. Srinivas, P. Ratnasamy, Sites for CO2 activation over amine-functionalized mesoporous Ti (Al)-SBA-15 catalysts, Microporous and Mesoporous Materials. 90 (2006) 314–326.

87. M. Gattrell, N. Gupta, A. Co, A review of the aqueous electrochemical reduction of CO2 to hydrocarbons at copper, Journal of Electroanalytical Chemistry. 594 (2006) 1–19. doi:10.1016/j.jelechem.2006.05.013.

88. S.S. Tan, L. Zou, E. Hu, Kinetic modelling for photosynthesis of hydrogen and methane through catalytic reduction of carbon dioxide with water vapour, Catalysis Today. 131 (2008) 125–129.

89. H. He, P. Zapol, L.A. Curtiss, Computational screening of dopants for photocatalytic two-electron reduction of CO2 on anatase (101) surfaces, Energy & Environmental Science. 5 (2012) 6196–6205.

90. M.A.A. Aziz, A.A. Jalil, S. Triwahyono, S.M. Sidik, Methanation of carbon dioxide on metal-promoted mesostructured silica nanoparticles, Applied Catalysis A: General. 486 (2014) 115–122.

91. V.P. Indrakanti, J.D. Kubicki, H.H. Schobert, Photoinduced activation of CO2 on Ti-based heterogeneous catalysts: Current state, chemical physics-based insights and outlook, Energy & Environmental Science. 2 (2009) 745–758. doi:10.1039/B822176F.

92. Z. Huang, K. Teramura, H. Asakura, S. Hosokawa, T. Tanaka, Efficient Photocatalytic Carbon Monoxide Production from Ammonia and Carbon Dioxide by the Aid of Artificial Photosynthesis, Chemical Science. (2017).

93. L. Zhang, W. Wang, D. Jiang, E. Gao, S. Sun, Photoreduction of CO2 on BiOCl nanoplates with the assistance of photoinduced oxygen vacancies, Nano Research. 8 (2015) 821–831. doi:10.1007/s12274-014-0564-2.

94. J. Lee, D.C. Sorescu, X. Deng, Electron-Induced Dissociation of CO2 on TiO2(110), Journal of the American Chemical Society. 133 (2011) 10066–10069. doi:10.1021/ja204077e.

95. L.-Y. Lin, Y. Nie, S. Kavadiya, T. Soundappan, P. Biswas, N-doped reduced graphene oxide promoted nano TiO2 as a bifunctional adsorbent/photocatalyst for CO2 photoreduction: Effect of N species, Chemical Engineering Journal. 316 (5) 449–460. doi:10.1016/j.cej.2017.01.125.

96. S. Xie, Y. Wang, Q. Zhang, W. Deng, Y. Wang, MgO- and Pt-Promoted TiO2 as an Efficient Photocatalyst for the Preferential Reduction of Carbon Dioxide in the Presence of Water, ACS Catalysis. 4 (2014) 3644–3653. doi:10.1021/cs500648p.

97. D. Zhao, J. Feng, Q. Huo, N. Melosh, G.H. Fredrickson, B.F. Chmelka, G.D. Stucky, Triblock Copolymer Syntheses of Mesoporous Silica with Periodic 50 to 300 Angstrom Pores, Science. 279 (1998) 548–552. doi:10.1126/science.279.5350.548.

98. F. Kleitz, S. Hei Choi, R. Ryoo, Cubic Ia3d large mesoporous silica: synthesis and replication to platinum nanowires, carbon nanorods and carbon nanotubes, Chemical Communications. (2003) 2136–2137. doi:10.1039/B306504A.

99. M.M. Shirolkar, H. Wang, AlFeO3 nanoparticles: An efficient perovskite material for low operating bias memristive devices, in: 2015: pp. 493–495. doi:10.1109/NANO.2015.7388646.

100. M. Shang, C. Zhang, T. Zhang, L. Yuan, L. Ge, H. Yuan, S. Feng, The multiferroic perovskite YFeO3, Applied Physics Letters. 102 (2013) 062903. doi:10.1063/1.4791697.

101. H. Tang, S. Chang, K. Wu, G. Tang, Y. Fu, Q. Liu, X. Yang, Band gap and morphology engineering of TiO 2 by silica and fluorine co-doping for efficient ultraviolet and visible photocatalysis, RSC Advances. 6 (2016) 63117–63130.

102. H. Liu, Z. Zhang, J. Meng, J. Zhang, Novel visible-light-driven CdIn2S4/mesoporous g-C3N4 hybrids for efficient photocatalytic reduction of CO2 to methanol, Molecular Catalysis. 430 (4) 9–19. doi:10.1016/j.molcata.2016.12.006.

103. R. Silva-Rodrigo, H. Castillo Jimenez, A. Guevara-Lara, J.A. Melo-Banda, A. Olivas Sarabia, A.I. Reyes de la Torre, F. Morteo Flores, A. Castillo Mares, Synthesis, characterization and catalytic properties of NiMoP/MCM41-γAl2O3 catalysts for DBT hydrodesulfurization, Catalysis Today. 250 (2015) 2–11. doi:10.1016/j.cattod.2014.09.007.

104. Y. Xu, M.A. Schoonen, The absolute energy positions of conduction and valence bands of selected semiconducting minerals, American Mineralogist. 85 (2000) 543–556.

105. M. Kruk, M. Jaroniec, C.H. Ko, R. Ryoo, Characterization of the Porous Structure of SBA-15, Chemistry of Materials. 12 (2000) 1961–1968. doi:10.1021/cm000164e.

106. R.A. Ortega-Domínguez, H. Vargas-Villagrán, C. Peñaloza-Orta, K. Saavedra-Rubio, X. Bokhimi, T.E. Klimova, A facile method to increase metal dispersion and hydrogenation activity of Ni/SBA-15 catalysts, Fuel. 198 (6) 110–122. doi:10.1016/j.fuel.2016.12.037.

107. T. Tsoncheva, L. Ivanova, J. Rosenholm, M. Linden, Cobalt oxide species supported on SBA-15, KIT-5 and KIT-6 mesoporous silicas for ethyl acetate total oxidation, Applied Catalysis B: Environmental. 89 (7) 365–374. doi:10.1016/j.apcatb.2008.12.015.

108. A. Tadjarodi, F. Zabihi, S. Afshar, Experimental investigation of thermo-physical properties of platelet mesoporous SBA-15 silica particles dispersed in ethylene glycol and water mixture, Ceramics International. 39 (2013) 7649–7655. doi:10.1016/j.ceramint.2013.02.103.

109. K. Kaneko, Determination of pore size and pore size distribution, Journal of Membrane Science. 96 (1994) 59–89. doi:10.1016/0376-7388(94)00126-X.

110. J.E. Castanheiro, I.M. Fonseca, A.M. Ramos, J. Vital, Tungstophosphoric acid immobilised in SBA-15 as an efficient heterogeneous acid catalyst for the conversion of terpenes and free fatty acids, Microporous and Mesoporous Materials. 249 (Enero 9) 16–24. doi:10.1016/j.micromeso.2017.04.047.

111. R. Evans, Fluids adsorbed in narrow pores: phase equilibria and structure, Journal of Physics: Condensed Matter. 2 (1990) 8989.

112. W.W. Lukens, P. Schmidt-Winkel, D. Zhao, J. Feng, G.D. Stucky, Evaluating Pore Sizes in Mesoporous Materials: A Simplified Standard Adsorption Method and a Simplified Broekhoff−de Boer Method, Langmuir. 15 (1999) 5403–5409. doi:10.1021/la990209u.

113. J. Ma, Q. Liu, D. Chen, S. Wen, T. Wang, Synthesis and characterisation of pore-expanded mesoporous silica materials, IET Micro & Nano Letters. 10 (2015) 140–144. doi:10.1049/mnl.2014.0413.

114. T. Kjellman, S. Asahina, J. Schmitt, M. Impéror-Clerc, O. Terasaki, V. Alfredsson, Direct observation of plugs and intrawall pores in SBA-15 using low voltage high resolution scanning electron microscopy and the influence of solvent properties on plug-formation, Chemistry of Materials. 25 (2013) 4105–4112.

115. B. Ma, L. Zhuang, S. Chen, Rapid synthesis of tunable-structured short-pore SBA-15 and its application on CO2 capture, Journal of Porous Materials. 23 (2016) 529–537.

116. M. Thommes, K. Kaneko, A.V. Neimark, J.P. Olivier, F. Rodriguez-Reinoso, J. Rouquerol, K.S. Sing, Physisorption of gases, with special reference to the evaluation of surface area and pore size distribution (IUPAC Technical Report), Pure and Applied Chemistry. 87 (2015) 1051–1069.

117. J.C. Groen, L.A. Peffer, J. Pérez-Ramírez, Pore size determination in modified micro- and mesoporous materials. Pitfalls and limitations in gas adsorption data analysis, Microporous and Mesoporous Materials. 60 (2003) 1–17.

118. M. Hussain, D. Fino, N. Russo, Development of modified KIT-6 and SBA-15-spherical supported Rh catalysts for N2O abatement: From powder to monolith supported catalysts, Chemical Engineering Journal. 238 (2) 198–205. doi:10.1016/j.cej.2013.06.032.

119. L. Vradman, L. Titelman, M. Herskowitz, Size effect on SBA-15 microporosity, Microporous and Mesoporous Materials. 93 (2006) 313–317.

120. G.H. Cedeño, R. Silva-Rodrigo, A. Guevara-Lara, J.A. Melo-Banda, A.I. Reyes de la Torre, F. Morteo Flores, A. Castillo-Mares, Role of the Si/Al molar ratio and pH in NIW/MCM41-Al2O3 catalysts for HDS of DBT, Catalysis Today. 271 (2016) 64–79. doi:10.1016/j.cattod.2015.10.024.

121. P.I. Ravikovitch, A. Vishnyakov, R. Russo, A.V. Neimark, Unified Approach to Pore Size Characterization of Microporous Carbonaceous Materials from N2, Ar, and CO2 Adsorption Isotherms, Langmuir. 16 (2000) 2311–2320. doi:10.1021/la991011c.

122. M. Hussain, P. Akhter, N. Russo, G. Saracco, Novel Ti-KIT-6 material for the photocatalytic reduction of carbon dioxide to methane, Catalysis Communications. 36 (2013) 58–62. doi:10.1016/j.catcom.2013.03.002.

123. P. Xiao, J. Hong, T. Wang, X. Xu, Y. Yuan, J. Li, J. Zhu, Oxidative Degradation of Organic Dyes Over Supported Perovskite Oxide LaFeO3/SBA-15 Under Ambient Conditions, Catalysis Letters. 143 (2013) 887–894. doi:10.1007/s10562-013-1026-2.

124. P.I. Ravikovitch, A.V. Neimark, Experimental Confirmation of Different Mechanisms of Evaporation from Ink-Bottle Type Pores: Equilibrium, Pore Blocking, and Cavitation, Langmuir. 18 (2002) 9830–9837. doi:10.1021/la026140z.

125. P. Gaudin, S. Dorge, H. Nouali, D. Kehrli, L. Michelin, L. Josien, P. Fioux, L. Vidal, M. Soulard, M. Vierling, M. Molière, J.-F. Brilhac, J. Patarin, Synthesis of Cu-Ce/KIT-6 materials for SOx removal, Applied Catalysis A: General. 504 (2015) 110–118. doi:10.1016/j.apcata.2014.11.024.

126. F. Zhang, Y. Zheng, Y. Cao, C. Chen, Y. Zhan, X. Lin, Q. Zheng, K. Wei, J. Zhu, Ordered mesoporous Ag-TiO2-KIT-6 heterostructure: synthesis, characterization and photocatalysis, Journal of Materials Chemistry. 19 (2009) 2771–2777. doi:10.1039/B818495J.

127. E. Beyers, E. Biermans, S. Ribbens, K. De Witte, M. Mertens, V. Meynen, S. Bals, G. Van Tendeloo, E.F. Vansant, P. Cool, Combined TiO2/SiO2 mesoporous photocatalysts with location and phase controllable TiO2 nanoparticles, Applied Catalysis B: Environmental. 88 (2009) 515–524.

128. S. Sun, X. Zhao, M. Yang, L. Wu, Z. Wen, X. Shen, Hierarchically ordered mesoporous Co3O4 materials for high performance Li-ion batteries, 6 (2016) 19564. doi:10.1038/srep19564.

129. F. Kleitz, F. Berube, R. Guillet-Nicolas, C.-M. Yang, M. Thommes, Probing adsorption, pore condensation, and hysteresis behavior of pure fluids in three-dimensional cubic mesoporous KIT-6 silica, The Journal of Physical Chemistry C. 114 (2010) 9344–9355.

130. J. Ding, K.-Y. Chan, J. Ren, F. Xiao, Platinum and platinum–ruthenium nanoparticles supported on ordered mesoporous carbon and their electrocatalytic performance for fuel cell reactions, Electrochimica Acta. 50 (2005) 3131–3141. doi:10.1016/j.electacta.2004.11.064.

131. V. Kocherbitov, V. Alfredsson, Assessment of porosities of SBA-15 and MCM-41 using water sorption calorimetry, Langmuir. 27 (2011) 3889–3897.

132. J. Liu, J. Yang, Q. Yang, G. Wang, Y. Li, Hydrothermally Stable Thioether-Bridged Mesoporous Materials with Void Defects in the Pore Walls, Advanced Functional Materials. 15 (2005) 1297–1302. doi:10.1002/adfm.200500122.

133. M.J. Reber, D. Brühwiler, Bimodal mesoporous silica with bottleneck pores, Dalton Transactions. 44 (2015) 17960–17967.

134. P. Xiao, L. Zhong, J. Zhu, J. Hong, J. Li, H. Li, Y. Zhu, CO and soot oxidation over macroporous perovskite LaFeO3, Catalysis Today. 258 (2015) 660–667.

135. H.-C. Yang, H.-Y. Lin, Y.-S. Chien, J.C.-S. Wu, H.-H. Wu, Mesoporous TiO2/SBA-15, and Cu/TiO2/SBA-15 composite photocatalysts for photoreduction of CO2 to methanol, Catalysis Letters. 131 (2009) 381–387.

136. Y. Zhao, L. Xu, Y. Wang, C. Gao, D. Liu, Preparation of Ti/ Si mixed oxides by sol–gel one step hydrolysis, Catalysis Today. 93 (2004) 583–588.

137. C. Jiang, K.Y. Lee, C.M.A. Parlett, M.K. Bayazit, C.C. Lau, Q. Ruan, S.J.A. Moniz, A.F. Lee, J. Tang, Size-controlled TiO2 nanoparticles on porous hosts for enhanced photocatalytic hydrogen production, Applied Catalysis A: General. 521 (2016) 133–139. doi:10.1016/j.apcata.2015.12.004.

138. D.R. Sahu, L.Y. Hong, S.-C. Wang, J.-L. Huang, Synthesis, analysis and characterization of ordered mesoporous TiO2/SBA-15 matrix: effect of calcination temperature, Microporous and Mesoporous Materials. 117 (2009) 640–649.

139. A. Avram, A. Radoi, V. Schiopu, M. Avram, H. Gavrila, Synthesis and characterization of γ-Fe2O3 nanoparticles for applications in magnetic hyperthermia, Synthesis. 10 (2011) 1.

140. Q. Li, S. Wang, Y. Yuan, H. Gao, X. Xiang, Phase-controlled synthesis, surface morphology, and photocatalytic activity of the perovskite AlFeO3, Journal of Sol-Gel Science and Technology. 82 (2017) 500–508.

141. F. Bérubé, A. Khadraoui, J. Florek, S. Kaliaguine, F. Kleitz, A generalized method toward high dispersion of transition metals in large pore mesoporous metal oxide/silica hybrids, Journal of Colloid and Interface Science. 449 (2015) 102–114. doi:10.1016/j.jcis.2014.12.001.

142. V. Jeyalakshmi, R. Mahalakshmy, K.R. Krishnamurthy, B. Viswanathan, Titania based catalysts for photoreduction of carbon dioxide: Role of modifiers, (2012).

143. T. Umebayashi, T. Yamaki, H. Itoh, K. Asai, Band gap narrowing of titanium dioxide by sulfur doping, Applied Physics Letters. 81 (2002) 454–456.

144. H.-S. Lee, C.-S. Woo, B.-K. Youn, S.-Y. Kim, S.-T. Oh, Y.-E. Sung, H.-I. Lee, Bandgap modulation of TiO 2 and its effect on the activity in photocatalytic oxidation of 2-isopropyl-6-methyl-4-pyrimidinol, Topics in Catalysis. 35 (2005) 255–260.

145. H.-Y. Wu, H. Bai, J.C.S. Wu, Photocatalytic Reduction of CO2 Using Ti–MCM-41 Photocatalysts in Monoethanolamine Solution for Methane Production, Ind. Eng. Chem. Res. 53 (2014) 11221–11227. doi:10.1021/ie403742j.

146. M. Gärtner, V. Dremov, P. Müller, H. Kisch, Bandgap widening of titania through semiconductor support interactions, ChemPhysChem. 6 (2005) 714–718.

147. R. van Grieken, J. Aguado, M.J. López-Muñoz, J. Marugán, Synthesis of size-controlled silica-supported TiO2 photocatalysts, Journal of Photochemistry and Photobiology A: Chemistry. 148 (2002) 315–322. doi:10.1016/S1010-6030(02)00058-8.

148. H. Lachheb, O. Ahmed, A. Houas, J.P. Nogier, Photocatalytic activity of TiO2–SBA-15 under UV and visible light, Journal of Photochemistry and Photobiology A: Chemistry. 226 (2011) 1–8. doi:10.1016/j.jphotochem.2011.09.017.

149. K. Kočí, L. Obalová, L. Matějová, D. Plachá, Z. Lacný, J. Jirkovský, O. Šolcová, Effect of TiO2 particle size on the photocatalytic reduction of CO2, Applied Catalysis B: Environmental. 89 (2009) 494–502.

150. C. Dette, M.A. Pérez-Osorio, C.S. Kley, P. Punke, C.E. Patrick, P. Jacobson, F. Giustino, S.J. Jung, K. Kern, TiO2 anatase with a bandgap in the visible region, Nano Letters. 14 (2014) 6533–6538.

# 7. APPENDIX

## 7.1. Pore size distribution

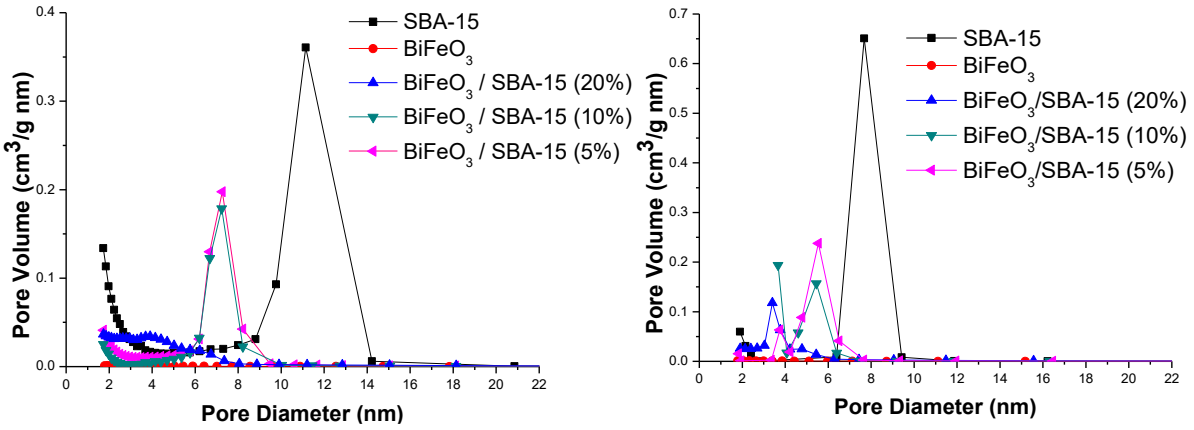


**Figure 40.** Pore size distribution of $BiFeO_3$/SBA-15 catalysts: adsorption (left) and desorption (right)

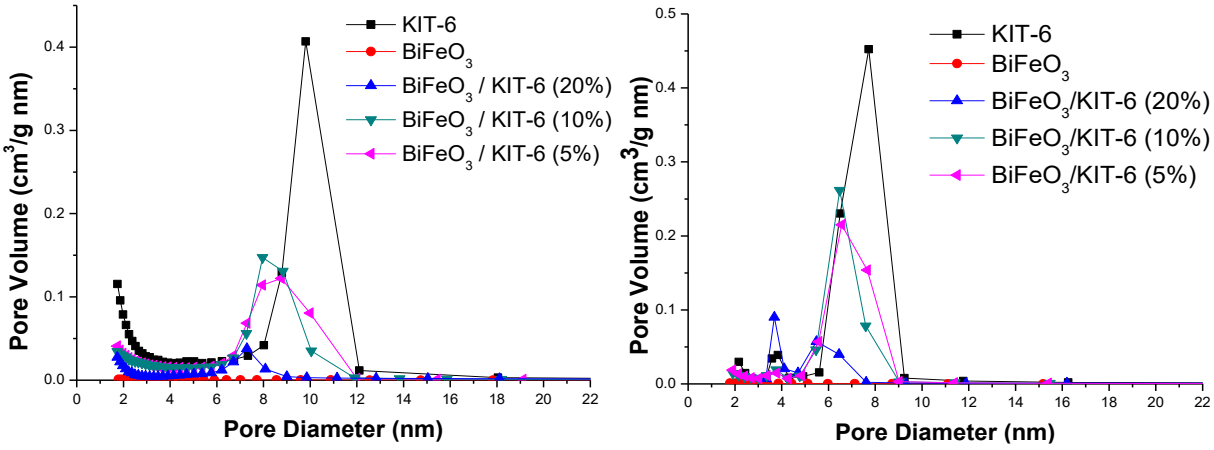


**Figure 41.** Pore size distribution of $BiFeO_3$/KIT-6 catalysts: adsorption (left) and desorption (right)

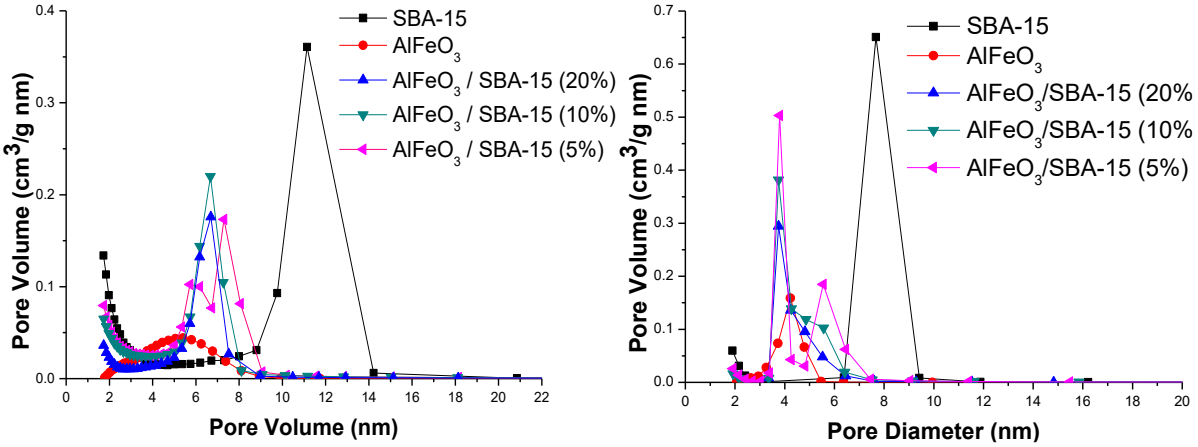


**Figure 42.** Pore size distribution of $AlFeO_3$/SBA-15 catalysts: adsorption (left) and desorption (right)

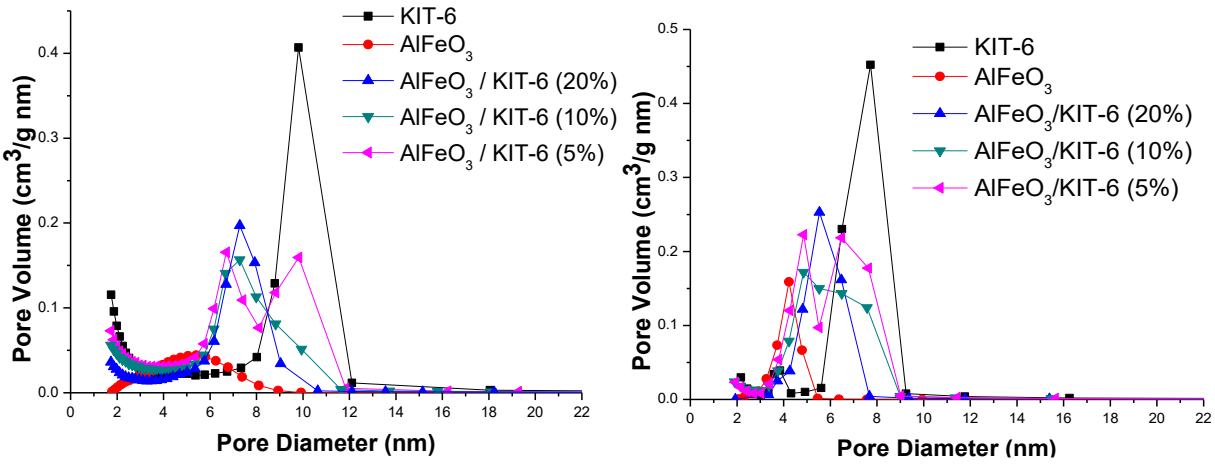


**Figure 43.** Pore size distribution of $AlFeO_3$/KIT-6 catalysts: adsorption (left) and desorption (right)

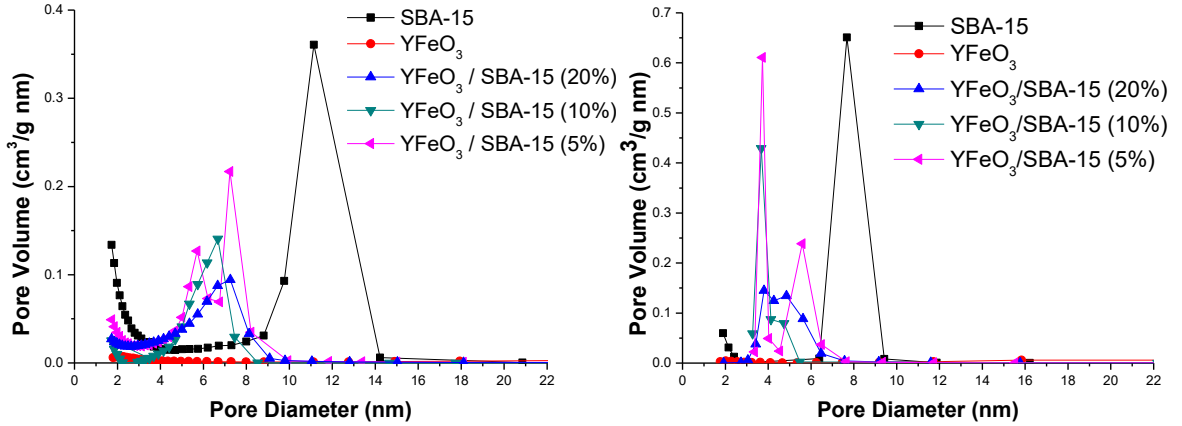


**Figure 44.** Pore size distribution of $YFeO_3$/SBA-15 catalysts: adsorption (left) and desorption (right)

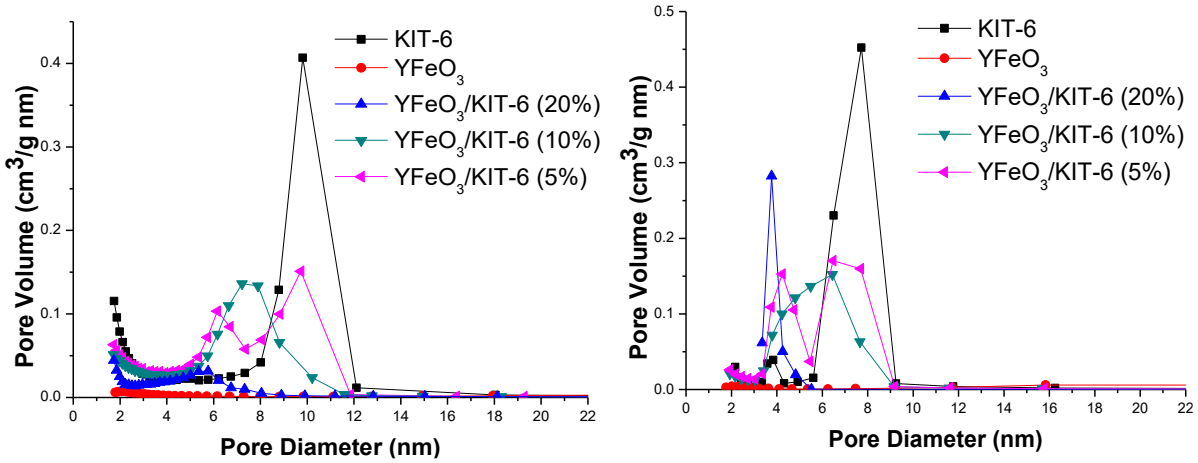


**Figure 45.** Pore size distribution of $YFeO_3$/KIT-6 catalysts: adsorption (left) and desorption (right)

## 7.2. Uv-Visible spectra

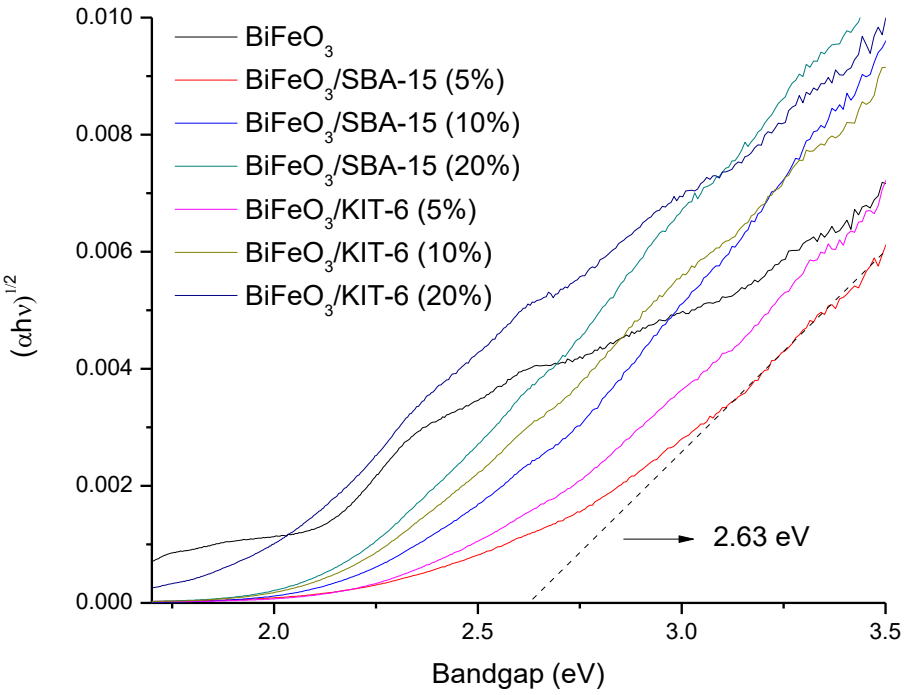


**Figure 46.** Uv-Vis spectrum of powder $LaFeO_3$ samples

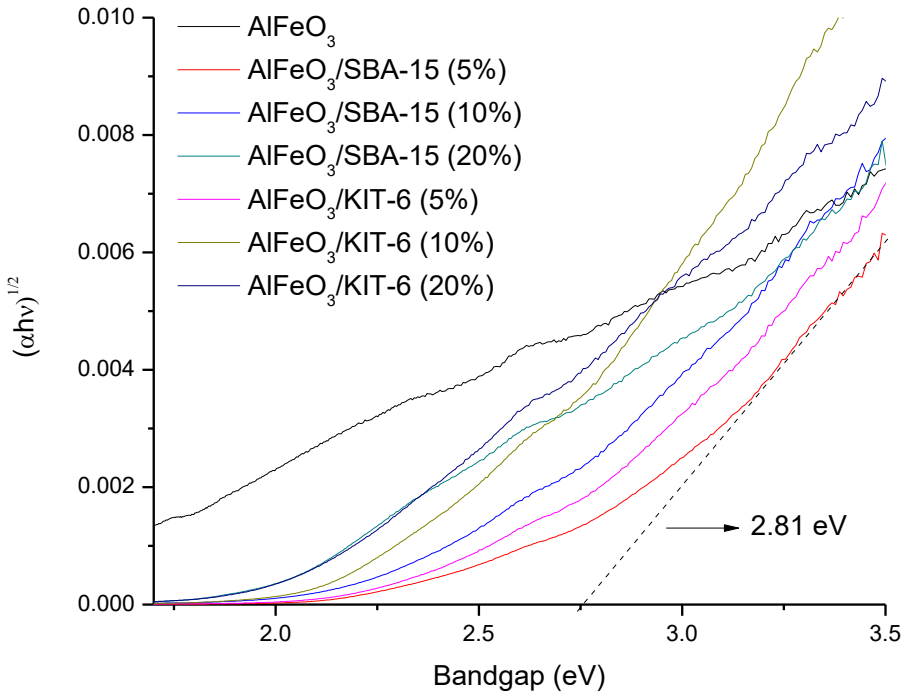


**Figure 47**. Uv-Vis spectrum of powder $AlFeO_3$ samples

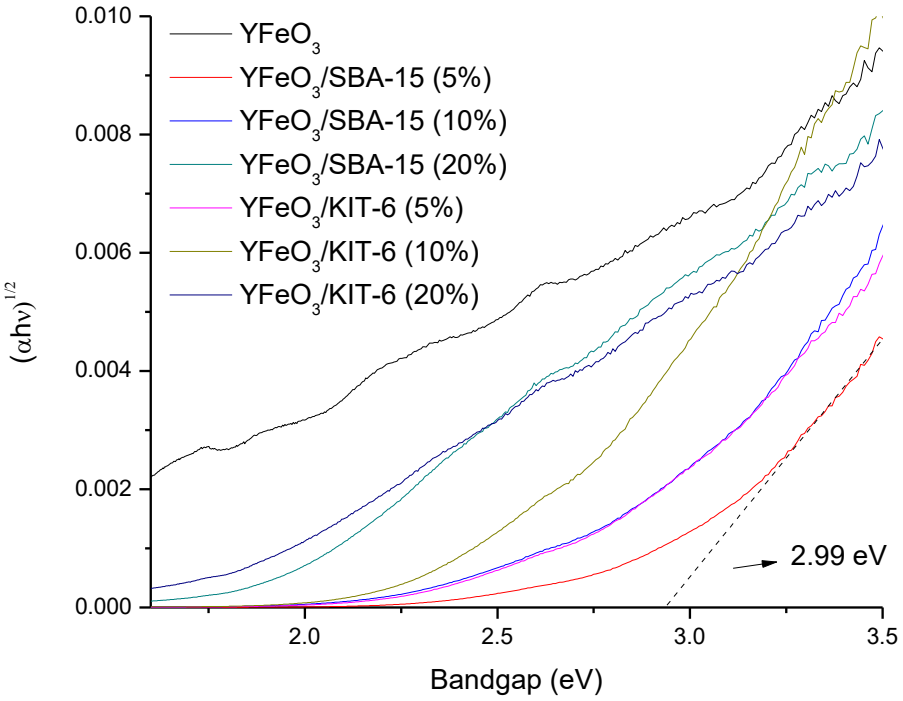


**Figure 48**. Uv-Vis spectrum of powder $YFeO_3$ samples